INVESTIGATING 3D SOLAR RADIATIVE CLOUD EFFECTS VIA MODIS

By

AMANDA R. GUMBER

A thesis submitted in partial fulfillment of

the requirements for the degree of

Master of Science

(Atmospheric and Oceanic Sciences)

at the

UNIVERSITY OF WISCONSIN-MADISON

2015

Thesis Declaration and Approval

I, Amanda R. Gumber, declare that this thesis titled 'Investigating 3D Solar Radiative Cloud Effects via MODIS' and the work presented in it are my own.

Amanda R. Gumber		
Author	Signature	Date

I hereby approve and recommend for acceptance this wok in partial fulfillment of the requirements for the degree of Master of Science:

Steven A. Ackerman		
Committee Chair	Signature	Date
Grant Petty		
Faculty Member	Signature	Date
Ankur Desai		
Faculty Member	Signature	Date

ABSTRACT

Cloud radiative feedbacks continue to be a primary source of uncertainty with respect to climate sensitivity in global climate models. This is often attributed to how clouds, their microphysical properties, and radiative processes are represented in these models. Much of the variability is caused by simplifications to the in-cloud microphysical properties and cloud morphology, and treatment of these properties as homogeneous. Satellite datasets provide daily measurements of cloud cover and their properties, which often can serve as model validation. This research seeks to investigate the 3D cloud radiative effects for both internal and external heterogeneity over the ocean through the use of MODIS Aqua and Terra satellites for a 10-year record. Internal heterogeneity is addressed through the use of a method that derives horizontal distributions of in-cloud properties while conserving the observed visible reflectance. This method corrects the horizontal distributions of cloud properties for possible filtered pixels from satellite algorithms. Sensitivities to the method are examined with respect to spatial and temporal variables as well as their relationship to areas with significant 3D cloud effects. A small satellite inter-comparison is also performed using PATMOS-x datasets using the method. External heterogeneity is addressed through the use of a metric to spatially identify heterogeneous scenes and use of the I3RC Monte Carlo radiative transfer model for one year. The I3RC model simulations compare the plane parallel assumption with the full 3D Monte Carlo as well as a comparison including the cloud property correction using the method described above. Future work to expand the model simulations and quantify the 3D effects is also discussed.

ACKNOWLEDGEMENTS

First, I would like to thank my research advisor, Dr. Michael Foster, for the opportunity to be a part of this research as well as his continual guidance and assistance throughout this project. I would also like to thank my academic advisor, Professor Steve Ackerman, for guidance and encouragement throughout my graduate career. I am also very appreciative of my thesis readers, Professor Grant Petty and Professor Ankur Desai. Thank you for taking the time to review my thesis and provide feedback.

I would also like to give a special thanks to the University of Wisconsin-Madison Department of Atmospheric and Oceanic Sciences. I've thoroughly enjoyed being a part of this department for both my undergraduate and graduate career. Thank you to all the faculty, staff, and students for making the past four years enjoyable.

And, finally, I would like to thank my family and friends for their endless love and support throughout my graduate school endeavors. I'd especially like to thank my parents for all their encouragement, love, patience, and hard work that has help me get where I am today.

TABLE OF CONTENTS

1. Introduction

1.1 Importance of Clouds and Remote Sensing for GCMs

Cloud feedbacks still remain a major source of uncertainty for climate sensitivity in general circulation models (GCM). One of the leading sources of this uncertainty is variability in solar radiation from changes in low-level marine cloud processes, which include shallow cumulus and stratocumulus topped boundary layer clouds (Webb et al. 2013). These types of clouds cover a vast amount of the Earth's oceans giving them an important role in regulating the Earth's energy budget, especially with respect to incident solar radiation. Approximately 30% of incoming solar radiation is reflected back to space from these clouds, which causes an overall net cooling effect at the surface. Studies have found that the variability of the solar radiative field in GCMs can be attributed to poor simulation of clouds including the neglect of the sub grid scale processes and cloud morphology, which encompass 3D radiative cloud effects (Cahalan et al. 1994a; Pincus and Klein 2000; Larson et al. 2001; Barker et al. 2003).

Satellite observations have been increasingly incorporated into 3D cloud effect studies since they more accurately portray daily cloud scenes and provide global data from multiple instruments. Satellite observations are used to identify cloud microphysical properties as well as providing a relationship between clouds and their radiative properties. Satellite instruments provide the only record of long-term global cloud observations that can provide validation for models. Satellite retrieval algorithms also refer to 1D radiative transfer for solving the inverse problem of satellite remote sensing. This can cause errors in retrieving optical thickness, an important cloud property often needed to derive other properties such as liquid water path depending on the instrument used. For this work, the Moderate Resolution

Imaging Spectroradiometer (MODIS) instrument is an imager that relies on optical depth retrievals and particle size to calculate LWP.

1.2 Biases from 1D Radiative Transfer

Many studies seek to quantify the magnitude of the bias in GCMs caused by the treatment of clouds as homogeneous. There are several variations in these results given the types of models used, specific regions chosen, individual cloud scenes selected, and time span of the study. These studies typically address either the effects of the in-cloud distributions of properties or the external cloud morphology. The bias caused from the neglect of in-cloud microphysical properties is referred to as the plane parallel albedo bias. The plane parallel albedo bias is calculated from the difference between the independent column approximation (ICA) and the standard 1D plane parallel calculations (Cahalan et al. 1994a). The ICA calculation consists of dividing a given grid box into several vertical columns and calculating the individual cloud properties for each smaller grid box. This approximation accounts for what shall be referred to as internal cloud heterogeneity. A variety of studies have been conducted to quantify the effects of the plane parallel albedo bias within models (Cahalan et al. 1994b; Marshak et al. 1998; Barker et al. 1999; Oreopoulos et al. 2004; Räisänen et al. 2004; Barker and Räisänen 2005). The results of the impacts of the plane parallel albedo bias vary from each study given the use of different types of cloud generating models such as a LES or a cloud-resolving model (CRM) with differing types of cloud scenes. Studies have also been conducted examining this bias with satellite data (Barker et al. 1996; Oreopoulos and Davies 1998; Pincus et al. 1999; Fu et al. 2000; Barker et al. 2003; Giuseppe and Tompkins 2003, 2005; Oreopoulos et al. 2007). Most importantly to this work, certain studies looked at the plane parallel bias for stratocumulus

clouds, which are the most homogeneous and closely resemble a plane parallel assumption. The results showed that even stratocumulus clouds are affected by this bias. In spite of the varying results, the studies all agreed that the plane parallel albedo bias does affect the radiative transfer, but in differing magnitudes and signs.

While the ICA method is able to capture the bias caused by the neglect of in-cloud properties, it does not account for horizontal photon transport between grid boxes. This bias can be referred to as the ICA bias(Cahalan et al. 1994a). In order to quantify the bias caused by the neglect of horizontal photon flow, the ICA bias can be described as the difference between a full 3D radiative transfer simulation and the ICA calculations. This bias accounts for the neglect of cloud morphology, which includes cloud shapes, cloud size, number of clouds, and distributions of clouds within a grid box. These variations of cloud field morphology are known as external cloud heterogeneity. Studies that examine external cloud heterogeneity have focused on the effects of cloud morphology on both heterogeneous and homogeneous clouds, cloud shadowing, enhanced illumination, horizontal photon flow, and the dependence on viewing geometry (Kobayashi 1989; Barker and Davies 1992; Zuev and Titov 1995; Marshak et al. 1998; Genkova and Davies 2003; O'Hirok and Gautier 2005; Liang et al. 2009; Girolamo et al. 2010). In connection to satellite measurements, studies have also aimed to spatially detect the difference between homogeneous and heterogeneous clouds as well as the effects of the viewing geometry (Kobayashi, 1993; Loeb and Davies, 1996; Loeb and Coakley, 1998) .

1.3 Challenges of Modeling Clouds in GCMs

Given that the horizontal resolution of commonly used GCMs ranges from 100-200 km, the variability of in-cloud properties must be parameterized to fit the much larger grid

box (*IPCC*, 2013). Studies using large eddy simulations (LES) of marine boundary layer clouds have shown that cloud properties such as cloud liquid water path (LWP) are sensitive to changes at horizontal resolutions of 100 m (Siebesma et al. 2003; Stevens et al. 2005). The microphysical properties of clouds remain an important part of research since certain aspects of cloud microphysical processes are still poorly understood. With respect to using GCMs for climate projections, a misrepresentation of cloud microphysical properties can lead to errors in atmospheric heating rates, cloud formation and dissipation, and precipitation rates. The larger grid boxes also neglect the spatial heterogeneity of cloud and atmospheric properties.

In order to obtain computationally efficient global model runs, some GCMs will simplify the radiative transfer to one vertical dimension, giving clouds and their boundary conditions a 1D plane parallel assumption. Using this assumption, cloud properties and atmospheric conditions are often based on mean values within the grid box. Parameterization and simplifications are used to estimate domain-averaged fluxes of 1D solar radiative transfer. Typically there are also separate parameterizations for liquid and ice clouds. Parameterizations have also been developed to account for vertical distributions of clouds based on various cloud overlap schemes, though active sensors have shown that certain assumptions in GCMs may over predict the overlap amount in subtropical ocean regions and land at high latitudes (Naud et al. 2008; Mace et al. 2009). The algorithms used to compute the radiative transfer of clouds is unrealistic given the clouds are assumed homogeneous and plane parallel while horizontal fluctuations between grid boxes are ignored. Advances in liquid water cloud representation incorporate model prediction of mass and number mixing ratio (Morrison and Gettelman 2008; Salzmann et al. 2010). Some models have developed methods to calculate microphysical processes while using subgrid cloud water variability

(Morrison and Gettelman 2008). While there has been progress to better parameterize the subgrid scale processes, this is still a continuing weakness in most GCMs causing biases due to misrepresenting the in-cloud microphysical properties and external shapes of cloud morphology.

1.4 Satellite Biases from 1D Radiative Transfer

Many recent satellite studies have explored the biases of using 1D radiative transfer to derive cloud microphysical properties on various cloud scenes (Horváth and Davies 2004; Kato et al. 2006; Kato and Marshak 2009; Girolamo et al. 2010; Ham et al. 2014). The effects of viewing geometry often the primary subject for these retrieval biases. As solar zenith angle increases, cloud optical depth measurements also tend to increase in research using the Earth Radiation Budget Satellite (ERBS) and MODIS instrument(Loeb and Coakley, 1998; Grosvenor and Wood, 2014) . For sensor zenith angle, MODIS cloud optical depth showed decreases the further the angle was from nadir (Várnai and Marshak 2007; Maddux et al. 2010). Satellite derived cloud effective radius has shown an opposite effect where an increasing sensor zenith angle is associated with increasing cloud effective radius (Maddux et al. 2010; Horváth et al. 2014). The study, Horvath et al. (2014) has considered whether the 3D effects can partially cancel each other out with respect to the liquid water path values, which are calculated from cloud effective radius and cloud optical depth. There are a variety of different results for each satellite instrument that derives cloud properties.

Distributions of satellite derived cloud properties can also be skewed depending on how an instrument decides what pixels are considered quality retrieval. MODIS uses a cloud mask to determine which pixels are considered cloudy (Ackerman et al., 1998; Ackerman et al. 2010). From this, an algorithm called the Clear Sky Restoral (CSR) algorithm performs a

series of quality checks to determine whether cloud property retrieval will be made for a specific pixel(King et al. 2006). Although the CSR algorithm does provide a filter for pixels that would be poor candidates for retrievals, there is room for error to filter pixels that are difficult to identify as clear or cloudy, which can affect the distributions of cloud properties. A method from Foster et al. (2011) that will be used later creates horizontal distributions of cloud properties while conserving the measured visible reflectance.

1.5 Study Objective

This study seeks to identify the 3D effects of both internal and external heterogeneity throughout the MODIS dataset. To examine internal heterogeneity, the method from Foster et al. (2011) is applied to generate horizontal distributions of liquid water path from visible reflectance measurements to compensate for pixel filtering. The effectiveness of the method is analyzed in comparison to using the MODIS retrieved cloud properties. Sensitivities to the method are explored with reference to viewing geometry, cloud spatial heterogeneity, and cloud amount. The method is also applied to a different satellite and processing algorithm. For external heterogeneity, a spatial heterogeneity index is applied to define the magnitude of heterogeneity (Liang et al. 2009). The study of external heterogeneity also includes full 3D Monte Carlo radiative transfer simulation for one year over an ocean region in the North Pacific to examine radiative differences between using a 1D plane parallel simulation and 3D Monte Carlo simulation. Additionally, the 3D Monte Carlo simulations apply the Foster et al. (2011) method to investigate radiative differences that can possibly occur from pixel filtering.

2. Data and Methodology

2.1 Introduction

In order to identify the different biases that arise from 3D radiative cloud effects, a few different metrics are applied. This study focuses primarily on using data from MODIS along with Pathfinder Atmospheres-Extended (PATMOS-X) processed data from the Advanced Very High Resolution Radiometer (AVHRR) instrument for comparison. To account for internal inhomogeneity, a method published by Foster et al. (2011) generates horizontal distributions of cloud microphysical properties over a grid box while conserving the scene visible reflectance. Other methods have explored using the statistical moments of cloud properties from satellite data to create probability distribution functions (PDF) to input into GCMs, but this can cause skewed distributions from pixel filtering. The goal of the method from Foster et al. (2011) is to create more accurate distributions of liquid water path throughout a grid cell that include potentially filtered pixels. This method will be referred to as the "fit method," where as the PDFs generated from the retrieved satellite data will be referred to as the "mask method."

With respect to external inhomogeneity, a metric that identifies homogeneous cloud fields (Liang et al. 2009), will be used as well as the International Comparison of 3-Dimensional Radiative Transfer Codes (I3RC) Monte Carlo model. The MODIS data is also fitted to 3D Monte Carlo model using a combination of the 1-km products. Both the fit and the mask method are applied to create input for the I3RC Monte Carlo Model to examine the radiative differences caused by pixel filtering along with comparison to a 1D plane parallel simulations.

2.2 MODIS

The MODIS instrument is located on the polar orbiting satellites, Aqua and Terra, which are a part of the NASA Earth Observing System mission. Terra has an orbit from north to south with an equatorial pass time in the morning where as Aqua has an orbit that passed from south to north with an afternoon equatorial pass time. Both satellites are able to obtain full data of the Earth's surface in 1-2 days. MODIS has 36 spectral bands ranging from 0.4 to 14.4 microns with spatial resolutions varying from 250 m to 1 km depending on the band used. All products used are from Collection 6.

2.2.1 Cloud Product (MY/OD06_L2)

The MODIS cloud product combines both visible and infrared radiances to solve for radiative and physical cloud properties. Used in this study, cloud optical thickness, cloud water path, effective radius, and cloud particle phase are derived from the visible, near-infrared, and shortwave infrared bands. Cloud top temperature and pressure are retrieved from the infrared bands (King et al. 1998).

2.2.2 Cloud Mask Product (MY/OD35_L2)

The MODIS Cloud Mask product uses an algorithm that employs a series of tests with visible and infrared thresholds (Ackerman et al. 1998; Ackerman et al. 2010). From this, confidence levels are assigned to each pixel with the broadest categories specifying confident clear, probably clear, probably cloudy, and cloudy. For this study, the cloud mask is used to determine which pixels are cloudy and determine cloud fraction over a larger area.

2.2.3 Calibrated Radiances (MY/OD021KM)

This product contains Level 1B calibrated and geolocated radiances for all 36 bands at 1 km. For this study, the visible reflectance channel (channel 1) measures from 0.62 to 0.67 microns.

2.2.4 Atmospheric Profile Product (MY/OD07_L2)

The atmospheric profile product is used to supply a profile of temperature and height for the 3D radiative transfer model. These profiles are produced at a 5 x 5 km resolution when at least 9 of the pixels are identified as cloud free. The temperature and height profiles are derived at 20 vertical levels using a clear sky synthetic regression retrieval algorithm.

2.2.5 Collection 6 Clear Sky Restoral

The clear sky restoral algorithm identifies which pixels are cloudy to retrieve optical and microphysical properties of clouds. The MODIS cloud mask product has certain pixels that are classified as probably cloudy and probably clear. The clear sky restoral algorithm identifies from those unclear pixels whether or not the pixel would be a poor retrieval candidate. If the algorithm finds the pixel to be a poor candidate, the pixel would be considered clear sky and no retrieval of optical or microphysical properties would be made. (King et al. 2006)

2.2.6 Geolocation Product (MY/OD03)

The geolocation product provides corresponding latitude and longitude coordinates for the 1 km data sources. It also provides solar and sensor zenith angles and solar and sensor azimuth angles for each 1 km grid cell.

2.3 PATMOS-x

The PATMOS-x dataset contains atmospheric and surface products from the AVHRR instrument. The AVHRR instrument has been aboard NOAA meteorological satellites since

1979. The instrument has 5 channels that range from solar to terrestrial infrared. Unlike MODIS, the visible reflectance channel has a larger span from 0.58-0.68 microns with a spatial resolution close to 1 km. The visible and near infrared channels are used to retrieve cloud optical depth and cloud effective radius. The infrared channel is used to retrieve cloud top temperature. The product also includes cloud mask and cloud phase. (Heidinger et al. 2014)

2.4 Horizontal Distributions of Cloud Properties conserving Scene Visible Reflectance

This method uses MODIS satellite measurements to calculate liquid cloud properties over partially cloudy scenes while conserving the total scene reflectance (Foster et al. 2011). Many times retrievals of cloud optical depth and effective radius are not attempted because of CSR identifying pixels as poor candidates for retrieval. Pixels often considered as poor candidates are dust and smoke particles, partially cloudy pixels, and sun glint. For some, cloud mask algorithm will still identify the pixel as cloudy, but they are given a missing value for their cloud property retrievals. In some cases due to the CSR, optically thin clouds or cloud edges are considered missing retrievals, which affects the distribution of the cloud microphysical properties.

The ocean from 60 degree N to 60 degree S is studied using MODIS data. The regions are then separated into 1 x 1 degree boxes, which are sampled at approximately 0.1-degree intervals. Ice clouds are also filtered out. The ocean regions are chosen because the surface emissivity of the ocean varies less than the surface emissivity over land. Many of the equations for the fit method rely on relationships with reflectivity values that are sensitive to variations of the surface albedo. Horizontal distributions of liquid water path will be

generated using the successful retrievals from MODIS (mask method) and derived distributions using a fit function between optical depth and visible reflectance (fit method).

2.4.1 Mask Method

The mask method refers to using only the successful cloud property retrievals made by the MODIS algorithms.

2.4.1.1 Liquid Water Path Calculation

The mask method obtains its cloudy pixels from the cloud mask. Only pixels that have cloud optical depth and near-cloud-top effective radius retrievals are used in order to calculate liquid water path. Equation 1 calculates liquid water path (Wood and Hartmann 2006). The density of liquid water is considered constant.

$$W = \frac{5}{9}\tau\rho_l r_{eff} \qquad (1)$$

2.4.1.2 Cloud Fraction Calculation

Cloud fraction is calculated from the cloud mask that indicates which pixels are defined as clouds. A ratio is formed for the number of pixels defined as clear divided by the total number of pixels within the 1 x 1 degree box. Subtracting this ratio from 1 will give the cloud fraction for the mask method.

2.4.2 Fit Method

The fit method refers to the methodology published in Foster et al. (2011) that aims to include the neglected optical retrievals from thin clouds and cloud edge pixel. The horizontal distributions are generated with respect to liquid water path, which is one of the main input variables for the 3D Monte Carlo radiative transfer model. This methodology can also be

used to create horizontal distributions of other cloud properties such as cloud optical depth and cloud effective radius. However, the focus of this study is strictly on liquid water path.

2.4.2.1 Liquid Water Path Calculation

Different from the mask method, the fit method calculates liquid water path based on a relationship between cloud optical depth and visible reflectance. From the cloud optical depth retrievals from MODIS, the relationship between the visible reflectance (R_{vis}) and retrieved optical depth (τ_{ret}) can be seen as the following, where a and b are coefficients that account for directional dependence from solar zenith angle, single-scattering albedo, and asymmetry parameters (e.g. Petty, 2006; Koren et al., 2008) :

$$R_{vis} = \frac{a\tau_{ret}}{1 + b\tau_{ret}} \qquad (2)$$

The left hand side of the equation is then expanded to include a geometric series for multiple scattering effects between the cloud and surface following a derivation from Koren et al. (2008):

$$R_{vis} = R_{vis} + \frac{c(1 - R_{vis})^2}{1 - cR_{vis}} \qquad (3)$$

The coefficients can be solved for by inserting the values of the cloud optical depth retrievals and observed visible reflectance into the equations listed above. Once the coefficients have values, the equation can be solved with respect to cloud optical depth. The observed visible reflectance for every pixel can be inserted into the equation to solve for cloud optical depth values for the entire sky.

A different equation must be used to solve for liquid water path other than Equation 1 because there are not effective radius values for each calculated cloud optical depth value. Using a method from Bennartz (2007), liquid water path can be calculated using a drop

number concentration, condensation rate, and cloud optical depth. Condensation rate is calculated from the following Equation 4, where $\frac{de_{sat}(T)}{dT}\frac{dT}{dz}$ is the derivative of the saturation vapor pressure with respect to temperature and saturated adiabatic lapse rate for an adiabatically ascending parcel. R_{H_2O} is the gas constant for water vapor.

$$c_w = 0.8\frac{1}{R_{H_2O}T}\frac{de_{sat}(T)}{dT}\frac{dT}{dz} \qquad (4)$$

Equation 5 calculates droplet number concentration, where k is the ratio between the volume mean radius and the effective radius to the third power and Q is the extinction efficiency. CF denotes cloud fraction. Droplet number concentrations and condensation rate are averaged over the 1 x 1 degree box and considered constants when calculating the individual pixel liquid water path.

$$N = \frac{2^{-5/2}}{k}\tau^3\left[\frac{W}{CF}\right]^{-5/2}\left[\frac{3}{5}Q\pi\right]^{-3}\left[\frac{3}{4\pi\rho_L}\right]^{-2}c_w^{1/2} \qquad (5)$$

The droplet number concentration can be approximated as a mean and considered a constant due to the small size of the spatial domain. The equation used to solve droplet number concentration can then be solved for liquid water path as seen in Equation 6. When using this equation to denote a single value of liquid water path, cloud fraction (CF) is assumed to be one.

$$W = \left[\frac{2^{-5/2}}{k}\frac{\tau_{fit}^3}{N}\left(\frac{3}{5}Q\pi\right)^{-3}\left(\frac{3}{4\pi\rho_l}\right)^{-2}c_w^{1/2}\right]^{2/5} \qquad (6)$$

2.4.2.2 Cloud Fraction Calculation

At this point there is a liquid water path measurement for every observed visible reflectance point, meaning there are values for both clear sky and cloudy sky. In order to

have an accurate distribution of liquid water path over each individual 1x1 degree box, these must be differentiated to separate the clear sky from the cloudy portion of the sky. Assuming a Gaussian distribution of clear sky reflectance, the clear sky can be subtracted from the total sky reflectance distribution. The center of the clear sky distribution is defined as the median of the clear sky reflectance values determined by the cloud mask. Any reflectance values less than the median of the clear sky reflectance is considered clear sky. A symmetric distribution is generated for the clear sky. The cloud fraction is solved using a ratio of the number of clear sky pixels from the symmetric distribution divided by the number of pixels in the total scene reflectance and subtracting from 1. Figure 1 shows an illustration of how clear sky is differentiated from cloudy sky over a scene.

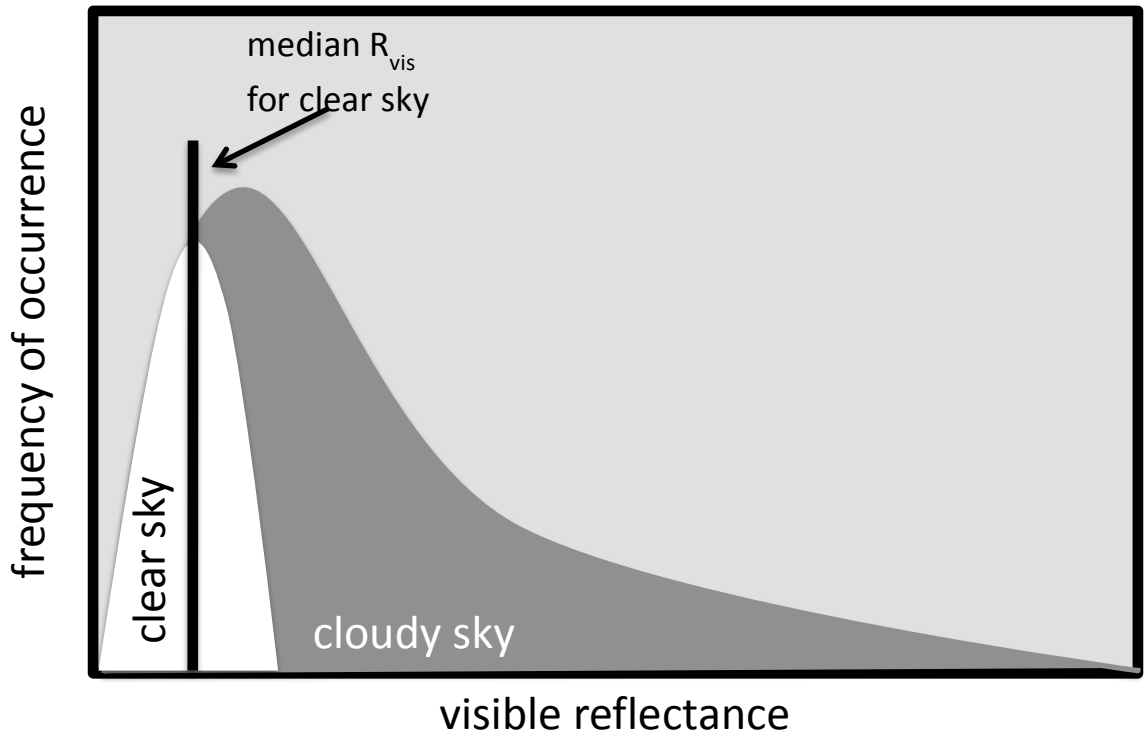

Figure 1. Illustration of distribution used to separate clear sky (white) from cloudy sky (gray) from Foster et al. (2011).

To create the distribution of liquid water path, the generated symmetric distribution of clear sky reflectance can be converted back to optical depth using the relationship of optical depth and visible reflectance established earlier in Equations 2 & 3. The clear sky optical depth values can be subtracted from the total fit derived values of optical depth and the cloudy sky optical depth values can be converted to liquid water path as described in Equation 6 for a calculation of a distribution of cloudy sky liquid water path.

2.4.3 PDFs of LWP

Once distributions of liquid water path are produced, the statistical moments of liquid water path are used to create probability distribution functions to identify the horizontal distribution and probability of occurrence for each 1 x 1 degree box. Both a gamma and Gaussian function can be applied for these distributions. The gamma function is the following from Heidinger (2003) where ν is the width parameter:

$$PDF(W) = \frac{1}{\Gamma(\nu)}\left(\frac{\nu}{\overline{W}}\right)^{\nu} W^{\nu-1} e^{-\left(\frac{W\nu}{\overline{W}}\right)} \qquad (7)$$

For the Gaussian function, a method is used in relating cloud geometric thickness to liquid water path in order to generate the probability distribution function (Considine et al. 1997; Wood and Hartmann 2006). The relationship between geometric thickness and liquid water path is derived from Equation 8 (Bennartz 2007).

$$W = 0.5 c_w H^2 \qquad (8)$$

First, the Gaussian distribution is generated as a function of geometric thickness. The probability density function of geometric thickness can then be converted into the probability density function of liquid water path from the relationship shown in Equation 9.

$$PDF(W) = PDF(H)\frac{dH}{dW} = \frac{1}{\sqrt{2c_w W}}PDF(H) \qquad (9)$$

2.4.4 Total scene reflectance calculation

The total scene reflectance for each 1 x 1 degree box can be calculated by using the cloud fraction, the mean reflectance of the cloudy portion and the mean reflectance of the clear portion (Equation 10).

$$\overline{R_{tot}} = CF(\overline{R_{cld}}) + (1 - CF)(\overline{R_{clr}}) \qquad (10)$$

The mean reflectance for the clear sky, $\overline{R_{clr}}$, is the mean of the clear pixels defined by the cloud mask. The mean reflectance for the cloudy portion of the sky, $\overline{R_{cld}}$, is determined by converting the probability density function of liquid water path into a probability density function of visible reflectance (Equation 11). This is done by taking the PDF of liquid water path and converting it back to a PDF of cloud optical depth, which was used earlier in Equation 6. The cloud optical depth distribution is converted back to reflectivity, and the mean of this distribution is used to solve the mean visible reflectance for the cloudy part of the sky.

$$\overline{R_{cld}} = \int_0^\infty R_{vis}\, PDF(W)dW \qquad (11)$$

Figure 2 shows a float chart describing the order of the steps and the equations used for both the mask and fit method to create horizontal distributions of liquid water path and derive the scene visible reflectance.

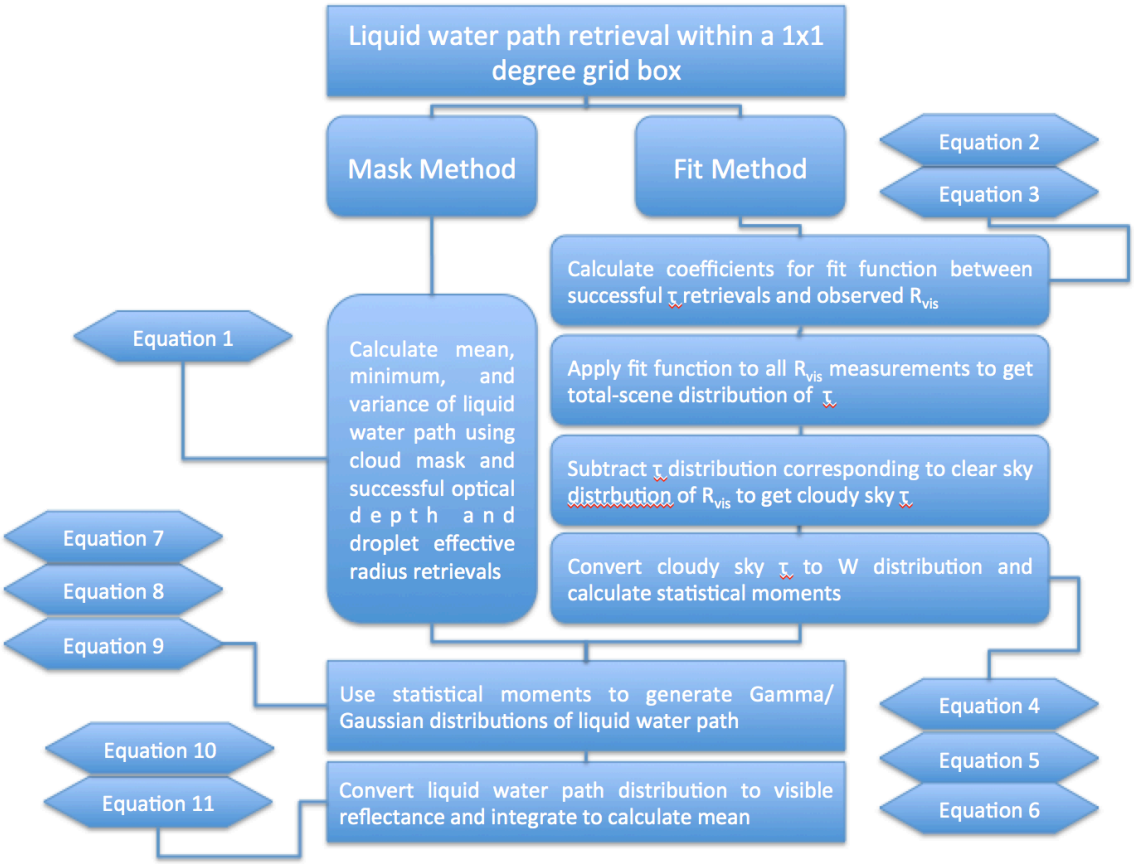

Figure 2. Float chart describing steps to calculate horizontal distributions of liquid water path and deriving visible reflectance for both the mask and the fit method. Modified from Foster et al. (2011)

2.5 Inter-comparison of 3D Radiation Codes (I3RC) Radiative Transfer Model

The I3RC radiative transfer model is a part of a project called the Inter-comparison of 3D Radiative Codes that began in the late 1990s. The goals of this project are to compare methods of various 3D radiative transfer calculations, publishing open source community 3D Monte Carlo code, providing benchmark results for testing of 3D radiative transfer codes, and delivering resources on radiative transfer. The model can be used to calculate radiances, radiative fluxes, and radiative heating rates for the top and the bottom of the specified domain within a cloudy atmosphere. With respect to this research, three main parts are used

to run the model, which include a scattering profile, creation of a domain of cloud properties, and a driver that performs Monte Carlo calculations (Pincus and Evans 2009).

The scattering profile program uses Mie theory to create a phase function table as a function of effective radius for a distribution of spherical particles. The particles are either identified as water, ice or aerosols. For the purpose of applying the fit methodology to 3D radiative transfer, the only particles that will be included are water particles since ice clouds are screened out from the analysis. The scattering properties of the water particles are averaged over the wavelengths 620 nm-670 nm, which is the interval of Band 1 for MODIS. The distribution of particle size can be calculated as either a gamma or lognormal distribution. The program calculates the phase function table along with extinction and single scattering albedo of the particles.

The cloud domain program reads in an ASCII file that has the properties of the clouds throughout the scene and formats the cloud input file along with the scattering profile to be used in the model. There are three different input files, which can be used in the model. All three input file types require the number of grid cells in each direction (x, y, z), the size of the grid cells, a height profile of the cell boundaries, and a temperature profile of the cell boundaries. The first input file type only requires the liquid water content (LWC) in each of the grid boxes. The second file type requires the LWC and effective radius. The third file type is for when using multiple types of particles, which requires a specification of particle type either as water, ice or aerosol, the mass content, and the effective radius. For this research, the first file type is currently being used to create input files.

There are a few assumptions being made to format the satellite data into a 3-dimensional scene for clouds. For the size of each grid box, one-kilometer MODIS data is

used. The height and temperature profiles are from the MODIS atmospheric profile product (MY/OD07_L2), which are retrieved for 20 vertical levels. From the MODIS cloud product (MY/OD06_L2), the cloud top height variable is used for identifying at which height the cloud top lies and is also used to calculate the height of the bottom of the cloud. The geometric thickness of the cloud is calculated by Equation 8 that uses liquid water path and a condensation rate (Equation 4), which is calculated from cloud top temperature (Bennartz 2007).

Cloud top temperature and cloud water path are also from the MODIS cloud product. The liquid water path is then distributed between the height levels it lies in and multiplied by distance between the height levels to give a LWC value. In order to create applicable scenes to run through the model, thresholds are set to not include any ice clouds, use scenes that are at least 10% cloudy but no more than 90% cloudy, and contain no missing reflectance values.

For the full 3D model scenes, a 10 x 10 km scene is created using the steps listed above for each 1 x 1 km grid box. Two separate scenes are created using both the liquid water path values supplied by the fit and the mask method. To create the 1D plane parallel scenes, one single grid box with spatial dimensions of 10 x 10 km is created using mean values of the LWC calculated by the fit and mask method as well as the other cloud parameters. The height and temperature profiles are a daily average over the specified ocean domain.

The Monte Carlo program runs a Monte Carlo simulation that calculates for each domain the outgoing fluxes for the top and bottom of the specified height profiles, absorption within the domain, intensity at the top and bottom of the domain for specified directions, and heating rate profiles. Assumptions made by the model are monochromatic solar radiative

transfer, uniform optical properties in each grid box, lambertian surface reflection, and periodic horizontal boundary conditions. Parameters that are input for the Monte Carlo simulations are solar zenith angle, azimuthal direction of photons, surface albedo, and the amount of photons to be used. Intensities are computed with respect to the sensor zenith angle and sensor azimuth angle.

3. Internal Heterogeneity

3.1 Introduction

Using the fit and mask methods, horizontal distributions of liquid cloud properties are generated over the ocean from 60 degree north to 60 degree south during the years 2003-2013. The validity of these distributions is assessed by how well the scene visible reflectance can be recreated. Sensitivities to the spatial and temporal variables such as geography, seasonality, cloudiness, scene heterogeneity, and viewing geometry are also explored. Internal heterogeneity is studied through using the horizontal distributions as well as its incorporation into the 3D modeling, which will be shown in the section 4. The fit and mask methodology will also be compared with the PATMOS-x processed AVHRR from NOAA-18 satellites, which has a comparable overpass times to Aqua, respectively. Additionally, PATMOS-x processed MODIS Aqua will also be compared.

3.2 Generation of Horizontal Distributions of Liquid Water Path

Horizontal distributions of LWP are generated for each 1 x 1 degree box as explained in section 2.4.3. Both a gamma and a Gaussian PDF were originally used to create these distributions. The initial results consistently showed that the Gaussian PDF was not able to recreate the scene visible reflectance as well as the gamma PDF, so the only the gamma PDF will be analyzed in this study.

Figure 3 shows scenes of different observed LWP distributions and their corresponding gamma PDF distribution for the fit and mask method using an array of different cloud fractions and mean LWPs. In general, the shape of the fit PDF agrees with the observed LWP distribution better than the mask generated PDF. There are a few instances where the observed LWP shows a smaller frequency of occurrence and the gamma-derived

distributions is skewed towards greater amount of LWP. The distributions with the largest cloud amounts (left column) tend to have a closer fit to their gamma-derived counterparts. The mask tends to do better when the observed distribution has a larger standard deviation.

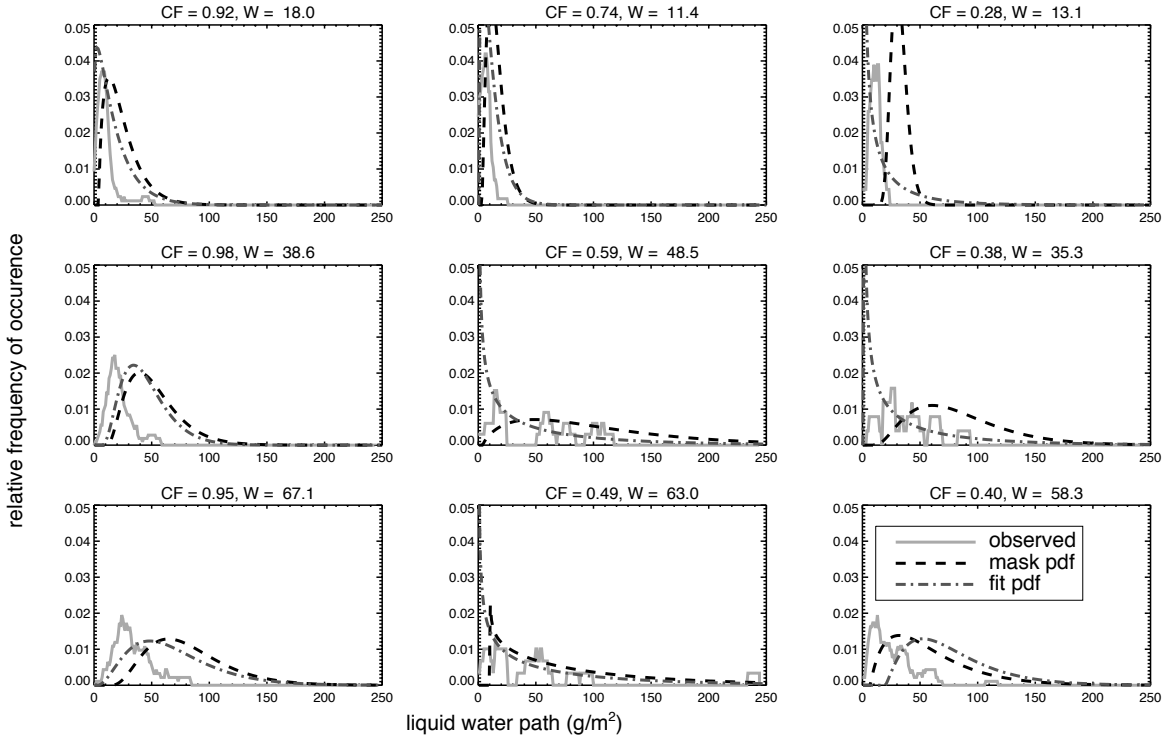

Figure 3. Relative frequency of occurrence for 1x1 degree distributions of liquid water path generated for an array of cloud fraction and liquid water path values for both the observed (solid gray) and the fit derived (dotted black) liquid water path distributions.

3.3 Global Liquid Water Path Adjustments

The scene measured mean LWP for the mask method corresponds to the satellite retrieved LWP from the MODIS algorithms, which includes the CSR. The global distribution of the mean LWP for all seasons show enhanced LWP along the ITCZ region in both the Pacific and Atlantic Oceans. There is seasonal increase of the mean LWP towards the north and south of the domain likely associated with midlatitude systems with highest LWP observed during each hemisphere's winter (Figure 4). Slightly lower amounts of LWP

are observed in the marine stratocumulus region off the coasts of California, Peru, and Angola. Aqua and Terra both show similar spatial patterns of the mean LWP, but the magnitude of the LWP for Aqua tends to be higher.

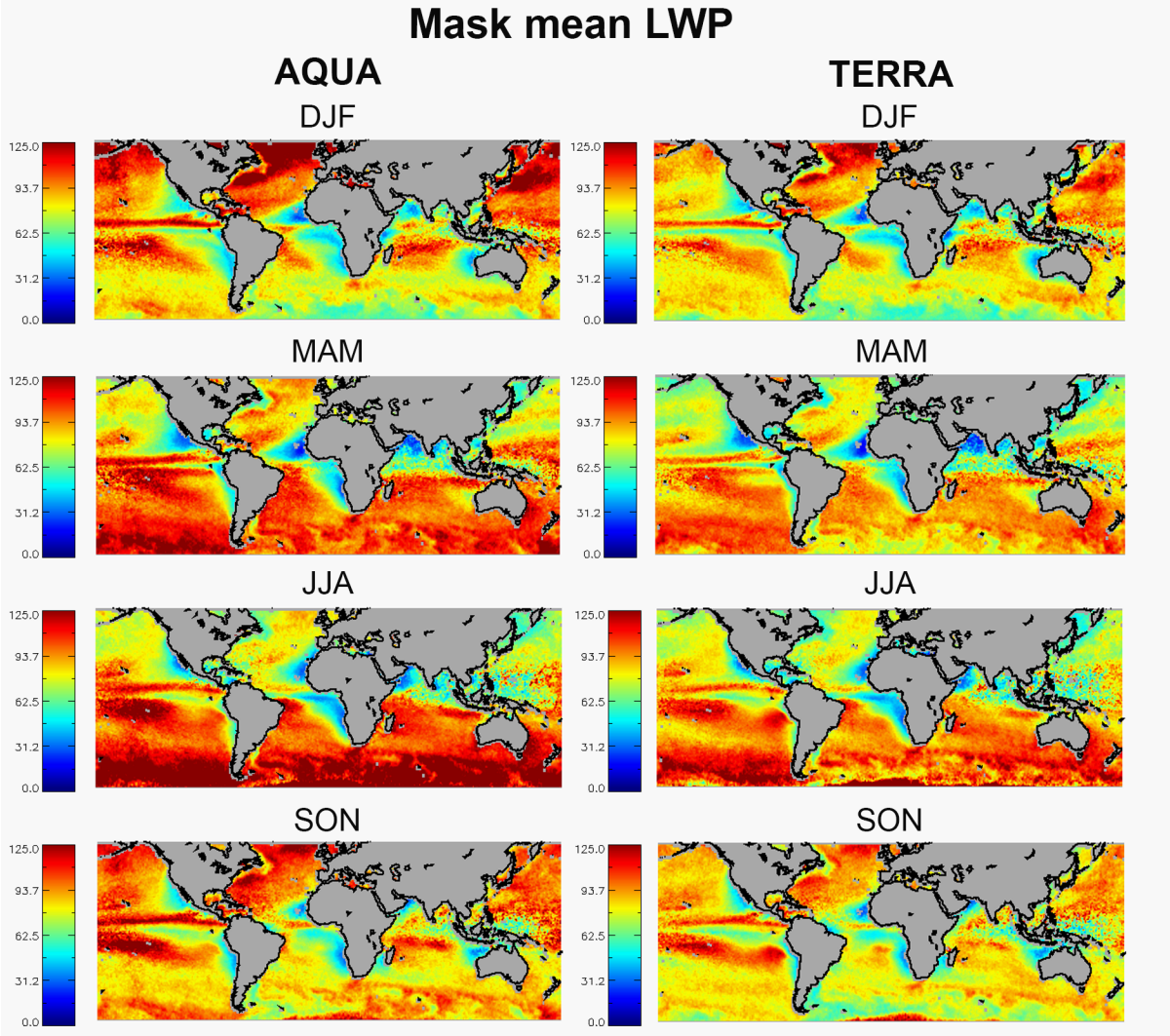

Figure 4. Aqua (left) and Terra (right) seasonal mask method mean liquid water path for 1x1 degree scenes measured in g/m^2

The fit method adjusts the mean LWP to account for potential pixels that do not have optical depth retrievals. This helps incorporate the optically thin or cloud edge pixels. As described previously in the methods section, the scene LWP is determined from a fit function between the observed visible reflectance and the retrieved cloud optical depth. The

application of the fit method lessens the total scene mean LWP (Figure 5). The highest values of the mean LWP are still observed in the ITCZ region, which remains constant throughout all the seasons. The southern hemisphere shows an increase of liquid water path from March to August with its peak occurring in the boreal summer months (June to August). The marine stratocumulus regions are visibly more apparent in comparison to the mask method. Similar to the mask method, Aqua tends to have overall higher values of the mean LWP than Terra.

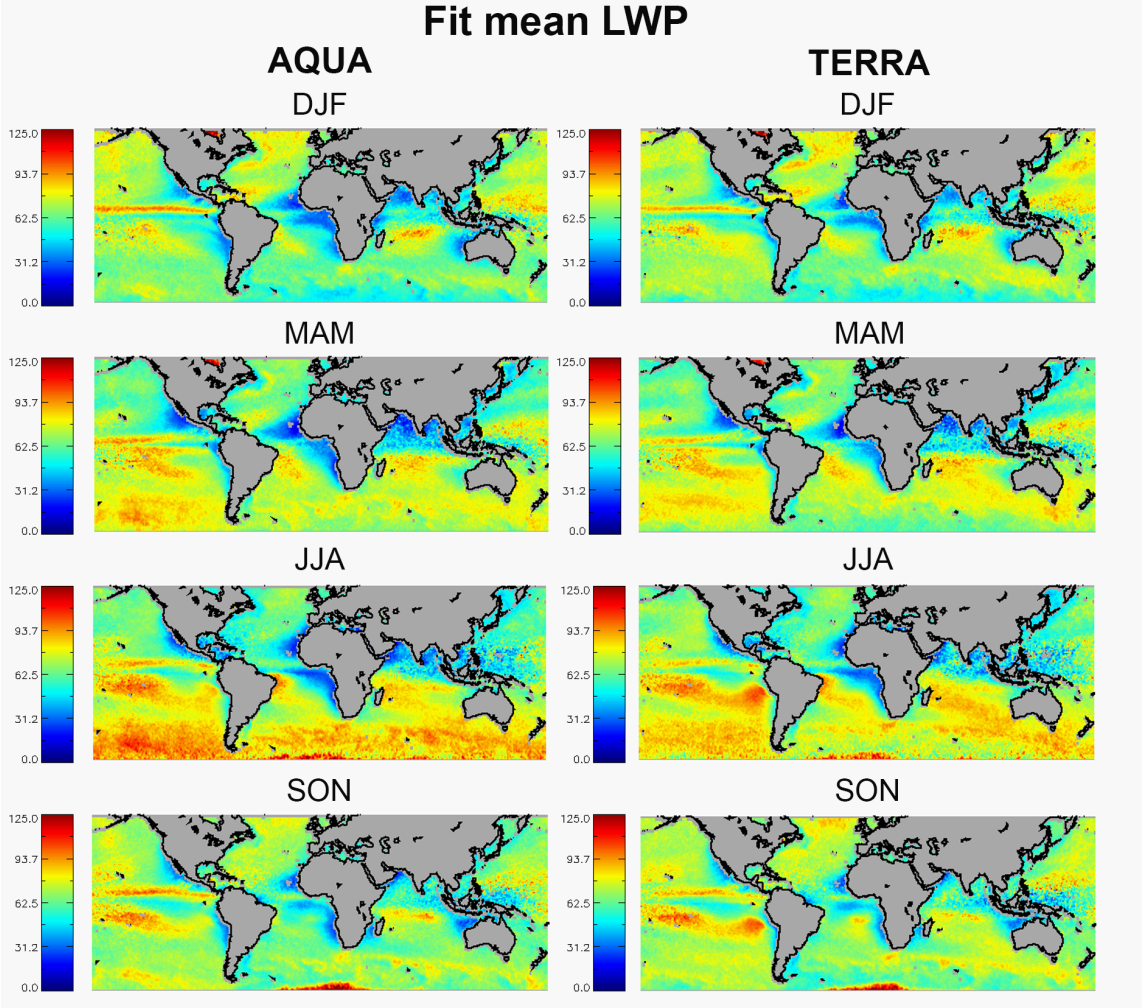

Figure 5. Aqua (left) and Terra (right) seasonal fit method mean liquid water path for 1x1 degree scenes measured in g/m^2

To better analyze the changes in the mean LWP, Figure 6 shows the mean LWP adjustment as a percentage change between the mask and the fit methodology. The region that experiences the largest adjustment is the ITCZ region, particularly in the areas where precipitation most often occurs. Through September to October, the northern hemisphere has the largest mean LWP adjustment with some reaching a 45% difference. The opposite occurs from March to August with the southern hemisphere exhibiting the largest adjustment. The least amount of change is experienced within the marine stratocumulus regions, which would be expected due to the more homogeneous nature of these clouds. Since the stratocumulus clouds are more uniform in shape and structure, fewer missing edge pixels and optically thin cloud are observed in scenes that contain them. The fit method adjusts the mean LWP values to lower than the mask method because the edge pixels and optically thin clouds are more likely associated with low LWP values.

Aqua shows an overall larger adjustment of LWP in comparison to Terra. This could possibly be linked to the cloud amounts present during the satellite overpass time. A study from King et al. (2013) that looked at the spatial and temporal distributions of clouds observed by both Aqua and Terra showed that the oceans tend to be cloudier during Terra's earlier overpass. With cloudier scenes, it is likely that there are less edge pixels or optically thin clouds to restore. With more cloud pixels detected, the fit method is likely to create a better fit function between the observed visible reflectance and retrieval optical depth measurements.

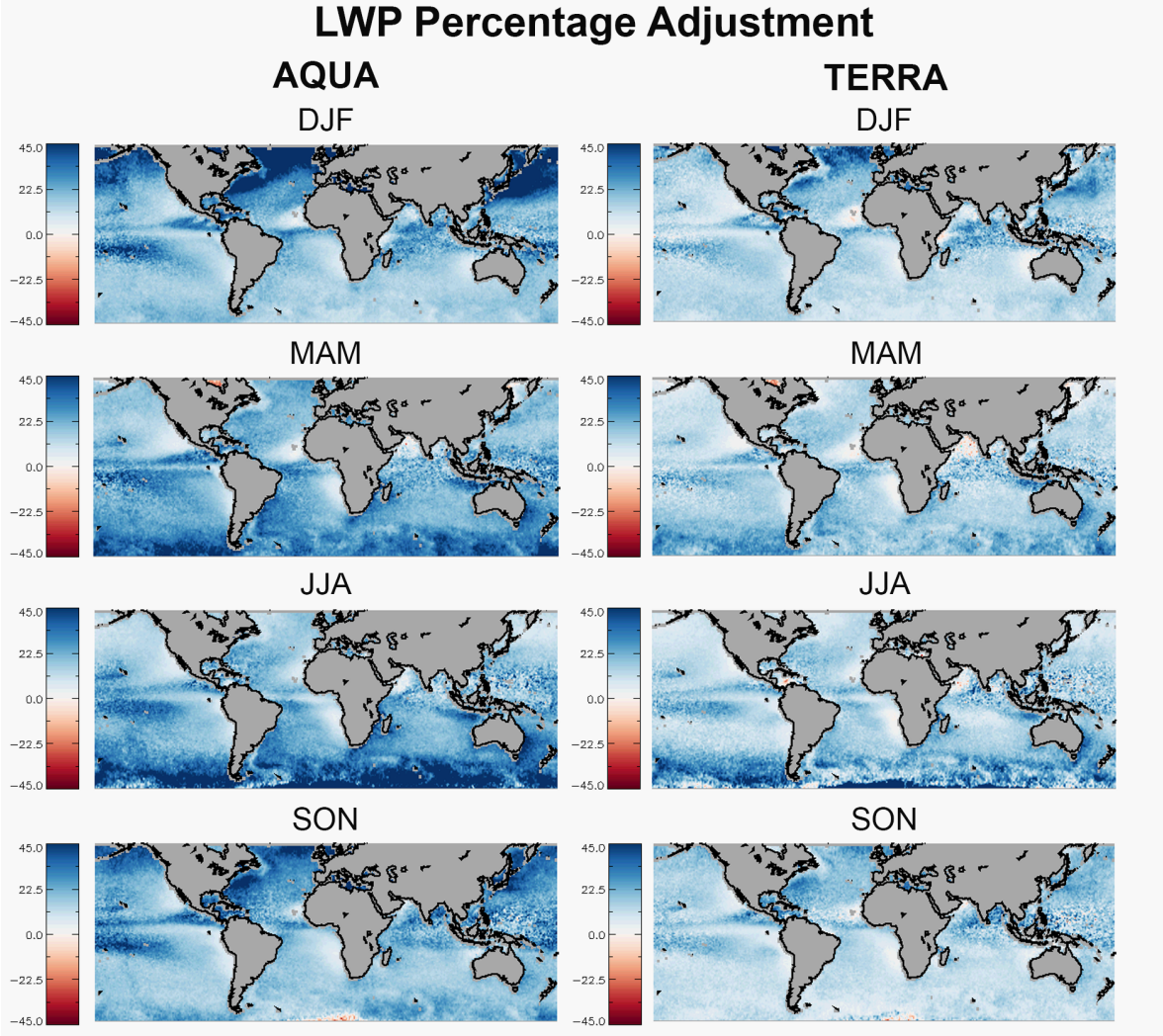

Figure 6. Aqua (left) and Terra (right) seasonal liquid water path percentage adjustment between the mask and fit method

3.4 Assessment of Mask and Fit methods

The ability to reconstruct the scene visible reflectance relates to the relationship between cloud optical properties and radiances in models. Often a model is evaluated based on how well the top of the atmosphere or surface radiances correspond to the observed reflectance from satellite data. Biases in the distribution of cloud properties will affect the model's capacity to reproduce the observed data. Therefore, the mask and fit method are assessed by the capacity to recreate the observed visible reflectance.

The mask method over the global ocean region from 2003 to 2013 from MODIS Aqua and Terra show an overall positive bias, indicating that the mask overestimates the visible reflectance (Figure 7). Spatially, Aqua and Terra show the same patterns with little deviation in the magnitude of the biases. Also, the magnitude of the bias adheres to a seasonal cycle. From December to February, the southern hemisphere summer shows a greater bias than the northern hemisphere, where as from June to August the northern hemisphere summer shows a greater bias than the southern hemisphere. March to May and September to October show the transition of the shift of the positive bias between the northern and southern hemisphere. Both instruments show a consistent overestimation of the derived visible reflectance.

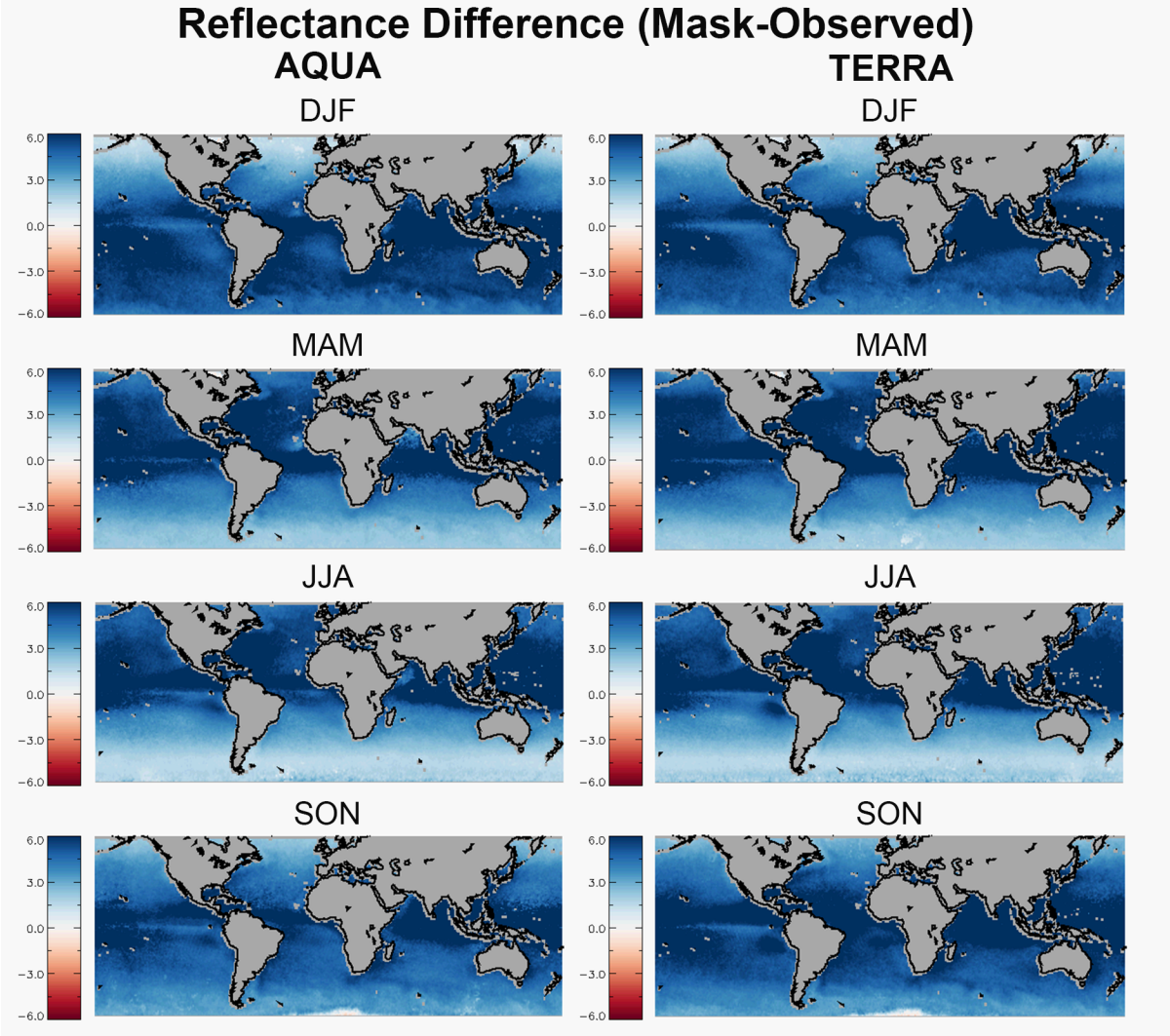

Figure 7. Seasonal difference between mask derived reflectance and observed reflectance for Aqua (left) and Terra (right)

When the fit method is applied globally over the oceans, the magnitude in the bias becomes significantly smaller for both Aqua and Terra in comparison to the mask method (Figure 8). The fit method shows spatially areas where there are both overestimations and underestimations. Generally, the seasonal cycle is no longer easily visible from using the fit calculations. Spatially, the fit method tends to underestimate the observed visible reflectance with much of the overestimation taking place over the tropics. Both satellites do show the regions of overestimation in the tropics, but the fit method shows noticeable differences

between both Aqua and Terra. At some points, Terra is slightly skewed towards the side of overestimation the observed visible reflectance, whereas Aqua tends to be marginally on the side of underestimating the visible reflectance. It is also important to note that the stratocumulus regions in the North Pacific, South Pacific and South Atlantic are located in regions of underestimation.

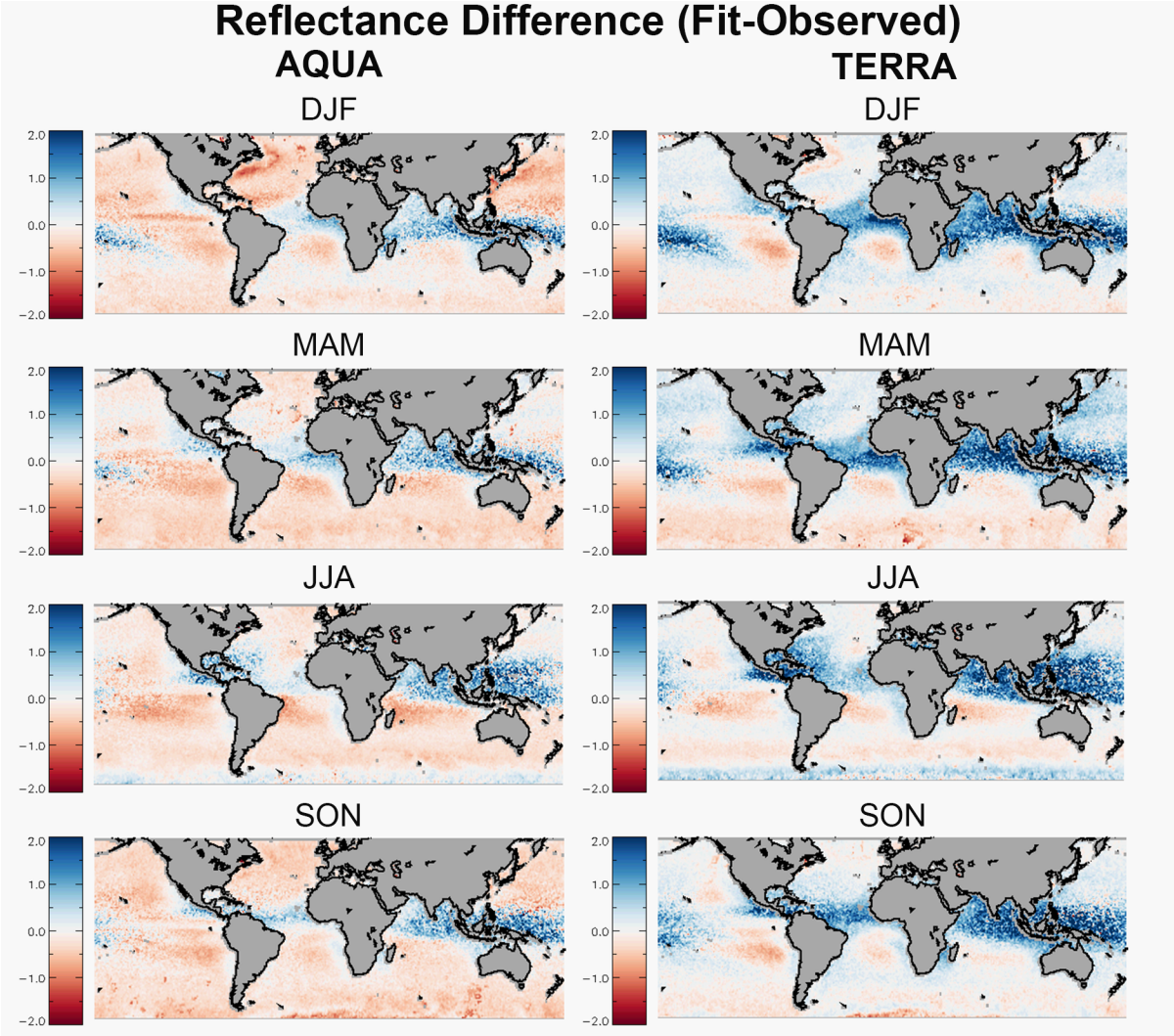

Figure 8. Seasonal difference between fit derived visible reflectance and observed reflectance for Aqua (left) and Terra (right)

To diagnose the existence of a potential seasonal cycle or the absence of one, monthly averages were taken of the percent bias of both the fit method and the mask method dividing

it between the northern and south hemisphere for both Aqua and Terra (Figure 9). Most notably, a seasonal cycle is shown for the mask method for both Aqua and Terra. The mask method always has a positive bias with the largest bias in the respective summer months for each hemisphere. Aqua tends to have a slightly smaller monthly bias than the mask method. The monthly bias for the fit method doesn't quite hold a seasonal cycle with the bias coming very close to zero. The bias for Aqua is slightly on the negative bias side, whereas Terra is slightly positive for the northern hemisphere and slightly negative for the southern hemisphere.

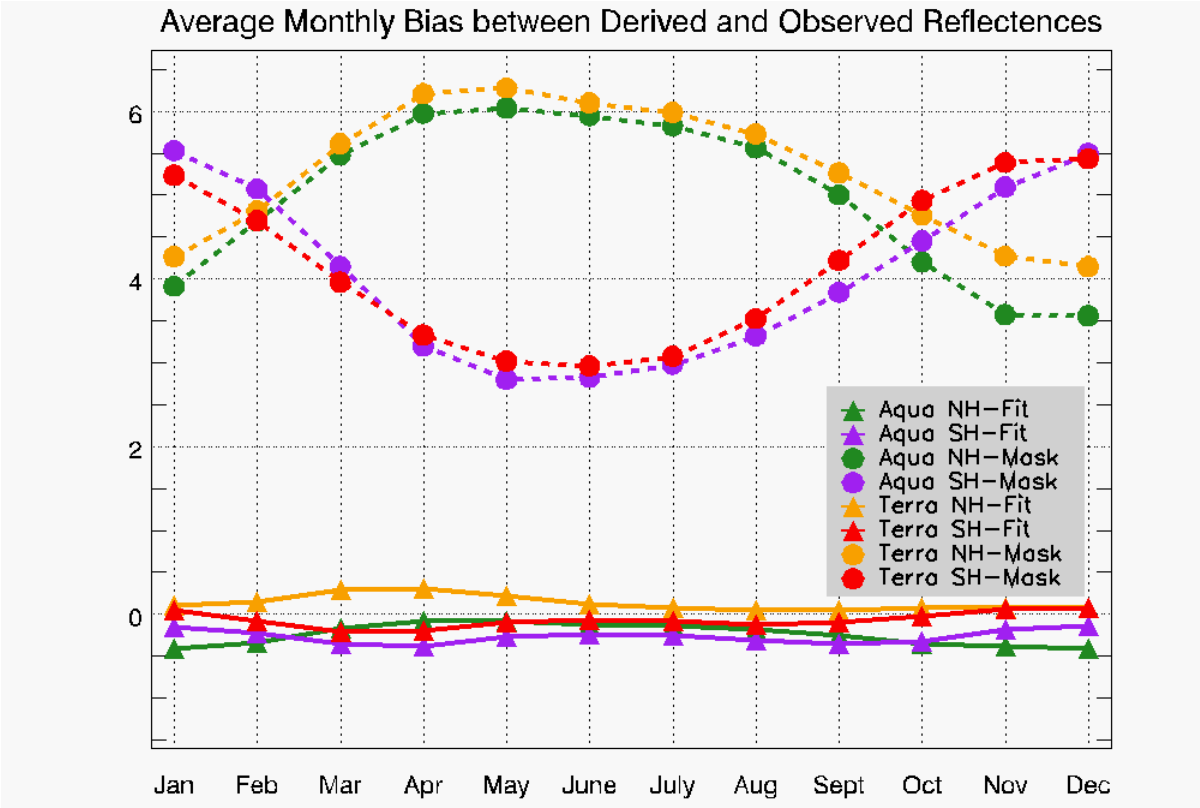

Figure 9. Average monthly bias between derived and observed reflectance for the mask (dotted, circle) and fit (solid, triangle) for the Aqua northern hemisphere (green) and southern hemisphere (purple) and Terra northern hemisphere (orange) and southern hemisphere (red)

From this the fit method can be seen as an overall improvement in comparison to the mask method given its ability to reconstruct the observed visible reflectance. To determine

spatially and temporally which areas experience the greater benefit of using the fit method in comparison to the mask method, Figure 10 shows the percentage improvement between the biases of the mask and the fit method. The largest improvements are seen over the tropics with maximum values reaching up to 15%, especially regions in the ITCZ that experience precipitation. The southern hemisphere shows more improvement from September to February, whereas the northern hemisphere shows the greatest amount of improvement from March to August. This is indicative of the smoothing out of the seasonal cycle that is shown by the mask method. Both Aqua and Terra show very similar amounts of improvement from using the fit method.

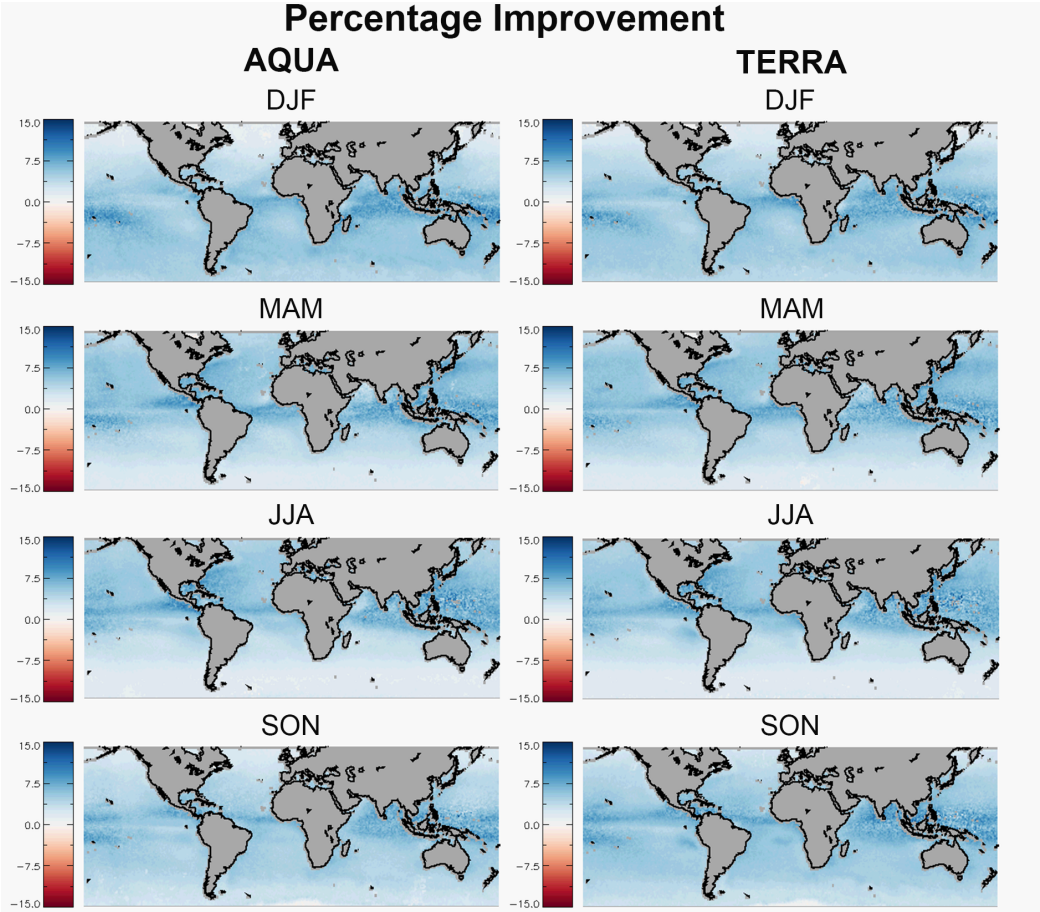

Figure 10. Seasonal percentage improvement from mask method to fit method for Aqua (left) and Terra (right)

3.5 Variable Sensitivities to Fit Method

Although the fit method significantly reduces the amount of bias in recreating the scene visible reflectance, certain regions show smaller biases of over- or under estimating the visible reflectance. The reasoning for this can possibly depend on certain variables that introduce sensitivity into the fit method. This section seeks to diagnose the characteristics of when the fit method best recreates the scene visible reflectance based on analysis of cloud fraction, viewing geometry, and cloud heterogeneity. The way these sensitivities are looked at is through using a 3D histogram to look at multiple variables at once. An example of interpreting this data is through Figure 11, which shows sensor zenith angle on the x-axis, solar zenith angle on the y-axis and cloud fraction on the vertical z-axis. The cubes are a measure of the bias between the fit derived visible reflectance and the observed visible reflectance. For instance, if a bin for sensor zenith angle of 50-60 degrees is chosen with a solar zenith angle bin of 10-20 degrees and a cloud fraction of 0 to 0.2, the bias for these parameters is approximately -2. The histograms were split up into northern and southern hemisphere to analyze any seasonal sensitivity.

3.5.1 Viewing Geometry and Cloud Fraction

The first relationship explored is that between viewing geometry and cloud fraction. The set up for this 3D histogram is sensor zenith angle on the x-axis, solar zenith angle on the y-axis and cloud fraction on the z-axis (Figure 11). One of the primary features seen for all seasons in the northern and southern hemisphere for Aqua is the greatest negative bias occurs at cloud fraction values below 0.2, which would indicate that the derived visible reflectance is too low. The greater the cloud fraction becomes the closer the bias gets to zero. Another noticeable trend at these lower cloud fractions is that the bias becomes greater as the

solar zenith angle decreases. There is a lack of points available for lower solar zenith and lower sensor zenith angles due to the filtering of sun glint.

Similar to Aqua, Terra shows the highest negative biases at cloud fractions below 0.2 for all viewing angles as well as the increase in the magnitude of the bias when approaching lower solar zenith angles (Figure 12). In the northern hemisphere from December-February, scenes with cloud fractions from 0.4 to 0.8 and mid range viewing angles from 30 to 50 degrees show a positive bias. The southern hemisphere from December to January shows a negative bias for all scenes with high viewing angles. From June to August, the scenes with cloud fractions above 0.2 show very little to no bias.

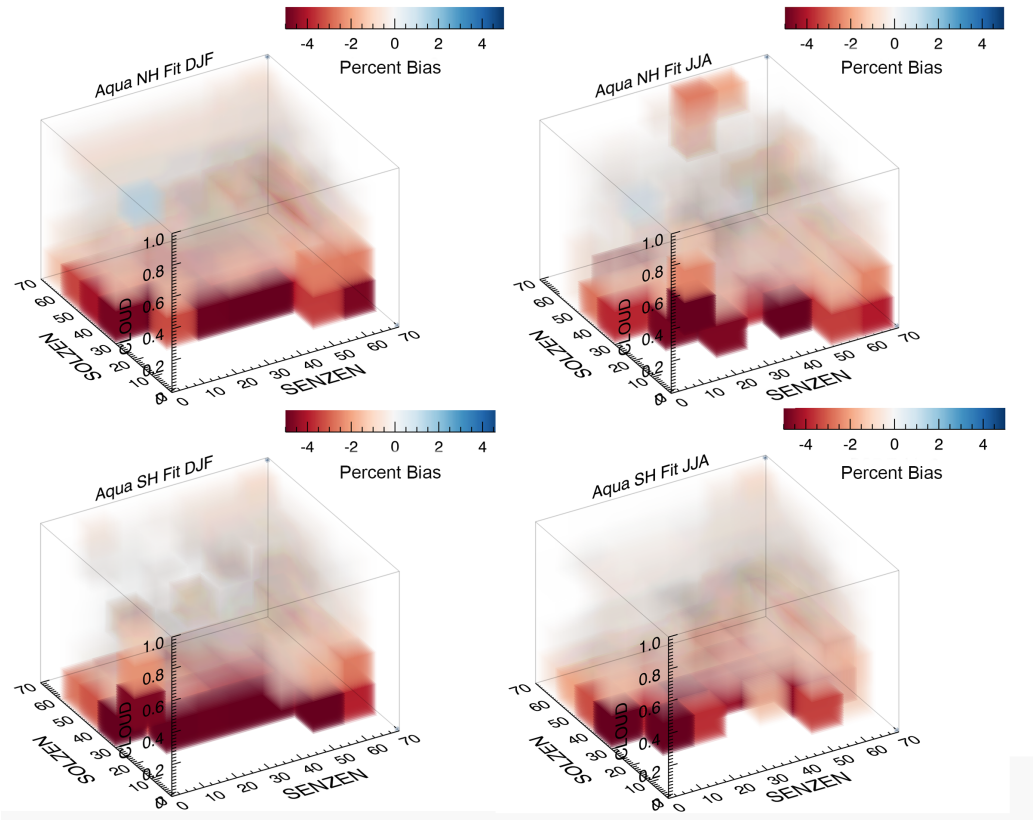

Figure 11. 3D histograms showing bias between fit derived reflectance and observed visible reflectance with respect to sensor zenith angle (x-axis), solar zenith angle (y-axis), and cloud fraction (z-axis) for Aqua DJF (left) and JJA (right) in the northern (top) and southern (bottom) hemisphere

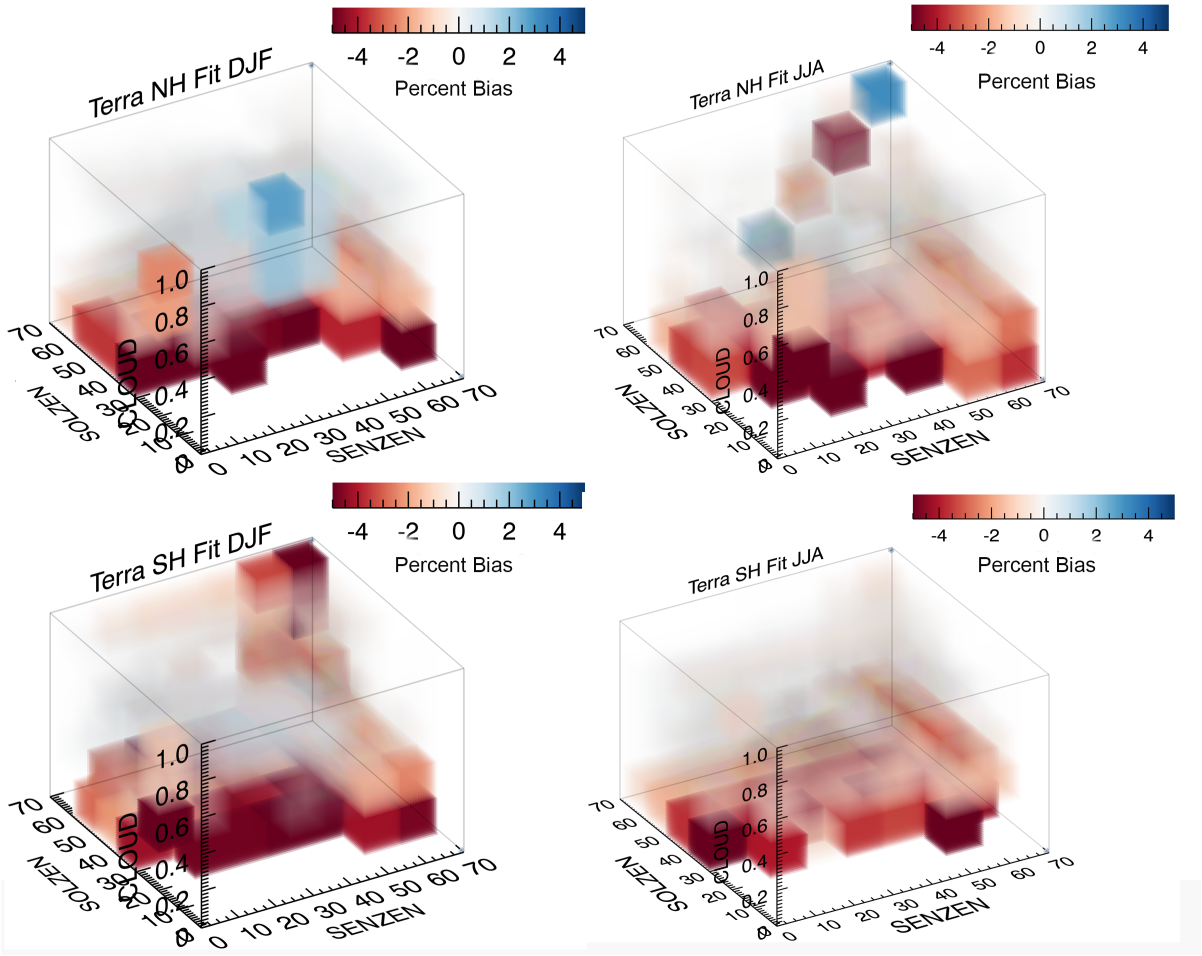

Figure 12. 3D histograms showing bias between fit derived reflectance and observed visible reflectance with respect to sensor zenith angle (x-axis), solar zenith angle (y-axis), and cloud fraction (z-axis) for Terra DJF (left) and JJA (right) in the northern (top) and southern (bottom) hemisphere

3.5.2 Cloud Heterogeneity, Solar Zenith Angle, and Cloud Fraction

Cloud heterogeneity is a metric that can be defined as the standard deviation of the visible reflectance in a scene divided by the mean scene visible reflectance to give a measure of how heterogeneous the cloud scene is (Liang et al. 2009). A high value indicates a heterogeneous cloud field and a low value indicates a more homogeneous cloud field.

The 3D histograms for Aqua do not show any particular seasonal sensitivity to the fit method though the 3D histograms reveal interesting relationships between cloud heterogeneity, solar zenith angle, and cloud fraction (Figure 13). The positive bias is seen for scenes with higher cloud fraction with either very high heterogeneity or very low heterogeneity. This suggests that for scenes that are overcast with either highly heterogeneous or highly homogeneous clouds the fit method overestimates the scene visible reflectance. At low cloud fractions, the fit method under-predicts for the entire range of solar zenith angles and cloud heterogeneity, but an increase in this negative bias is seen as heterogeneity increases and the closer the solar zenith angle moves towards nadir. Unique to the northern hemisphere for December to February, there seems to be a noticeable outlier for a negative bias at higher cloud fractions, high cloud heterogeneity, and only for solar zenith angle bins of 10-20 and 60-70 degrees.

Terra shows observations similar to Aqua. The major difference is for scenes with high cloud fraction, high heterogeneity, and a range of solar zenith angles (Figure 14). Aqua showed a large positive bias for these variables. In contrast, Terra has a mixture of both positive and negative biases with the negative biases occurring in the highest heterogeneity bin of 1.0 to 1.2 and the next lowest cloud heterogeneity bin from 0.9 to 1.0 showing positive biases. Both Aqua and Terra show the least amount of bias for mid-range cloud heterogeneity (0.2-0.9), mid range cloud fractions (0.2-0.8) and for the entire range of solar zenith angles where there are not missing values.

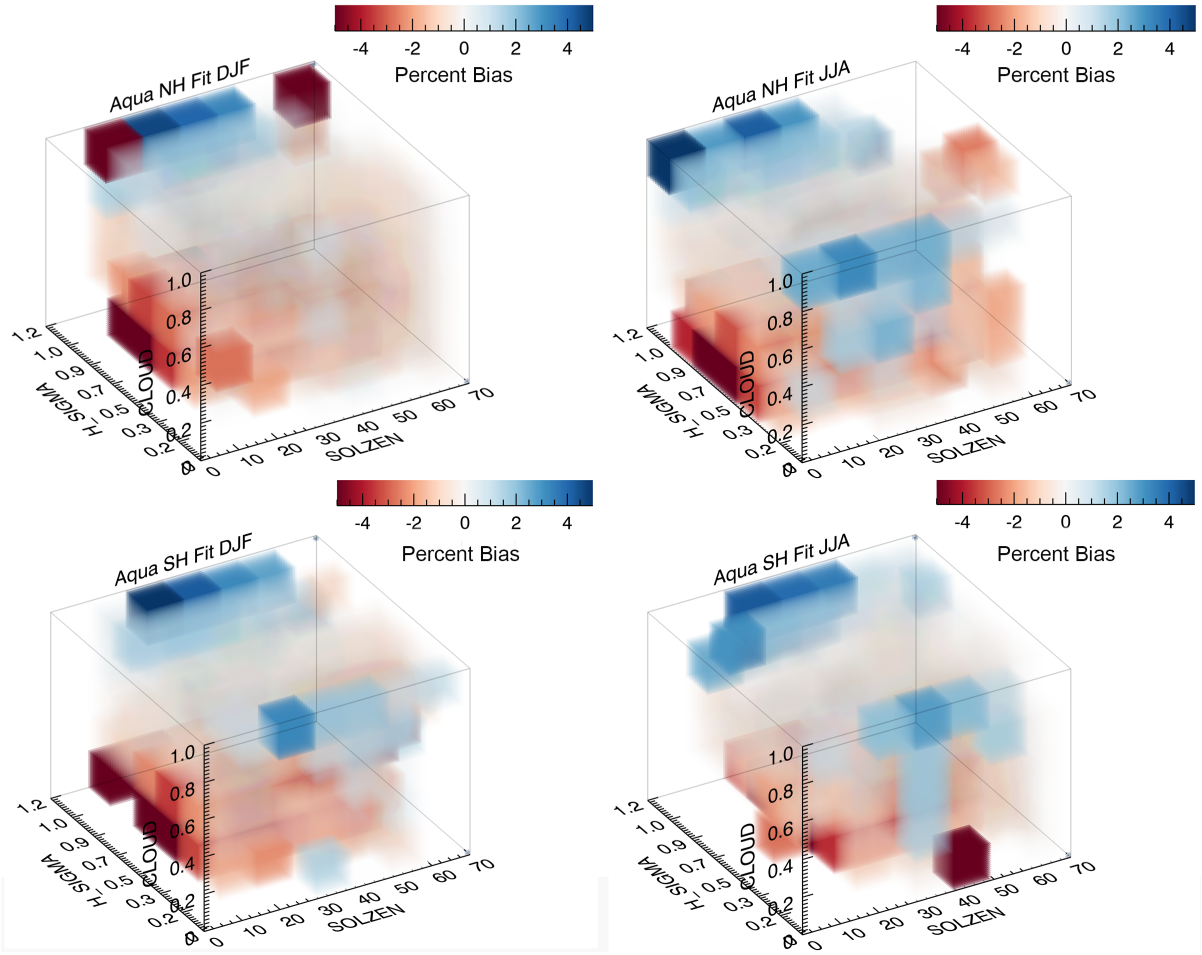

Figure 13. 3D histograms showing bias between fit derived reflectance and observed visible reflectance with respect to solar zenith angle (x-axis), cloud heterogeneity (y-axis), and cloud fraction (z-axis) for Aqua DJF (left) and JJA (right) in the northern (top) and southern (bottom) hemisphere

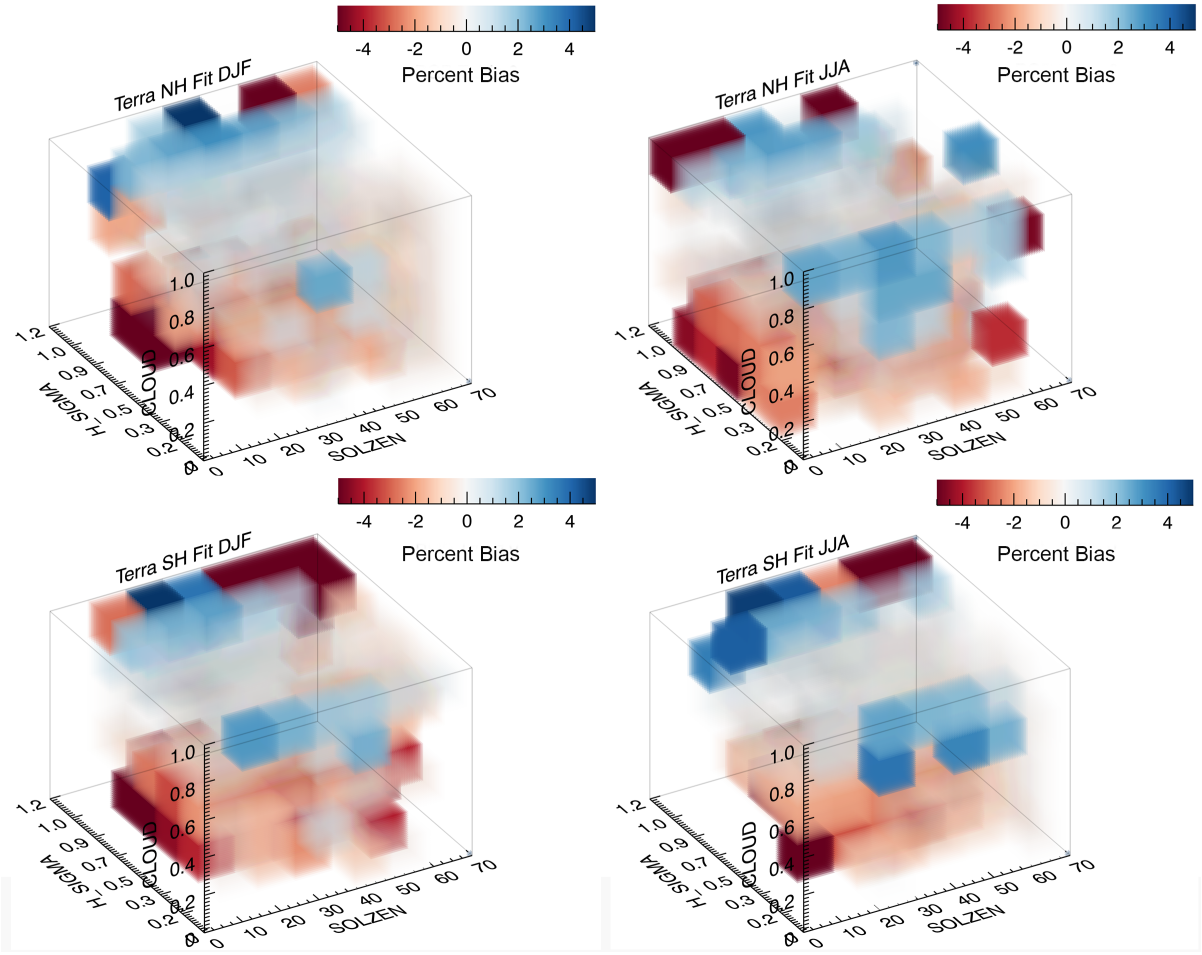

Figure 14. 3D histograms showing bias between fit derived reflectance and observed visible reflectance with respect to solar zenith angle (x-axis), cloud heterogeneity (y-axis), and cloud fraction (z-axis) for Terra DJF (left) and JJA (right) in the northern (top) and southern (bottom) hemisphere

3.5.3 Cloud Heterogeneity, Sensor Zenith Angle, and Cloud Fraction

With the combination of cloud heterogeneity, sensor zenith angle, and cloud fraction, Aqua shows a slight amount of seasonality between the northern and southern hemisphere. In the northern hemisphere, December to January show a negative bias for lower cloud fractions (0.0 – 0.4) with the peak of the negative bias seen around sensor zenith angles closest to nadir and mid-range cloud heterogeneities between 0.5 to 0.9 (Figure 15). Similar to the previous histograms in sections 3.5.2 showing cloud heterogeneity, cloud fraction, and solar

zenith angle, a positive bias is seen at high cloud heterogeneities and high cloud fractions, though for the northern hemisphere winter there are some negative biases that show up in this same area. The northern hemisphere summer shows a similar trend to the northern hemisphere winter for scenes with lower cloud fractions. At higher cloud fractions, there is a positive bias for high cloud heterogeneity and low cloud heterogeneity that does not show a dependence on sensor zenith angle. The southern hemisphere summer corresponds very well with the northern hemisphere summer suggesting a slight seasonality between these relationships. The southern hemisphere winter is comparable to the northern hemisphere with the exception of the high cloud fractions scenes with high cloud heterogeneities only have a positive bias.

Terra shows very similar patterns to Aqua with minor differences (Figure 16). The northern hemisphere and southern hemisphere winters have a negative bias at scenes with lower cloud fraction values, sensor zenith angles closest to nadir and mid range heterogeneities. While at higher cloud fractions, there is a positive bias for high cloud heterogeneities with the exception of a negative bias around sensor zenith angles of 0-10 and 50-70 degrees. For the northern and southern hemisphere summers, the same biases are seen in likeness to the winter with the only contrast being seen for high cloud fraction scenes with low cloud heterogeneity showing positive biases.

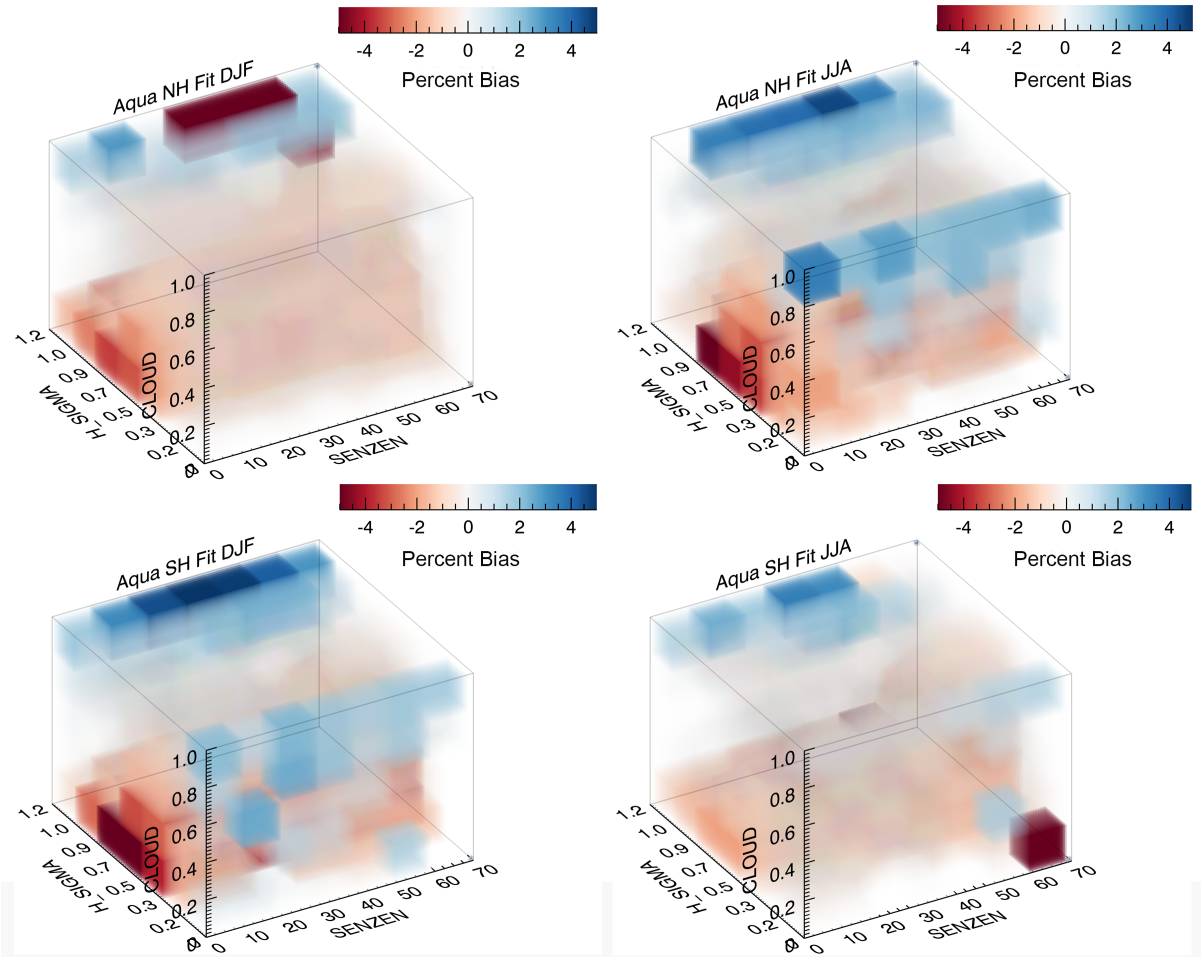

Figure 15. 3D histograms showing bias between fit derived reflectance and observed visible reflectance with respect to sensor zenith angle (x-axis), cloud heterogeneity (y-axis), and cloud fraction (z-axis) for Aqua DJF (left) and JJA (right) in the northern (top) and southern (bottom) hemisphere

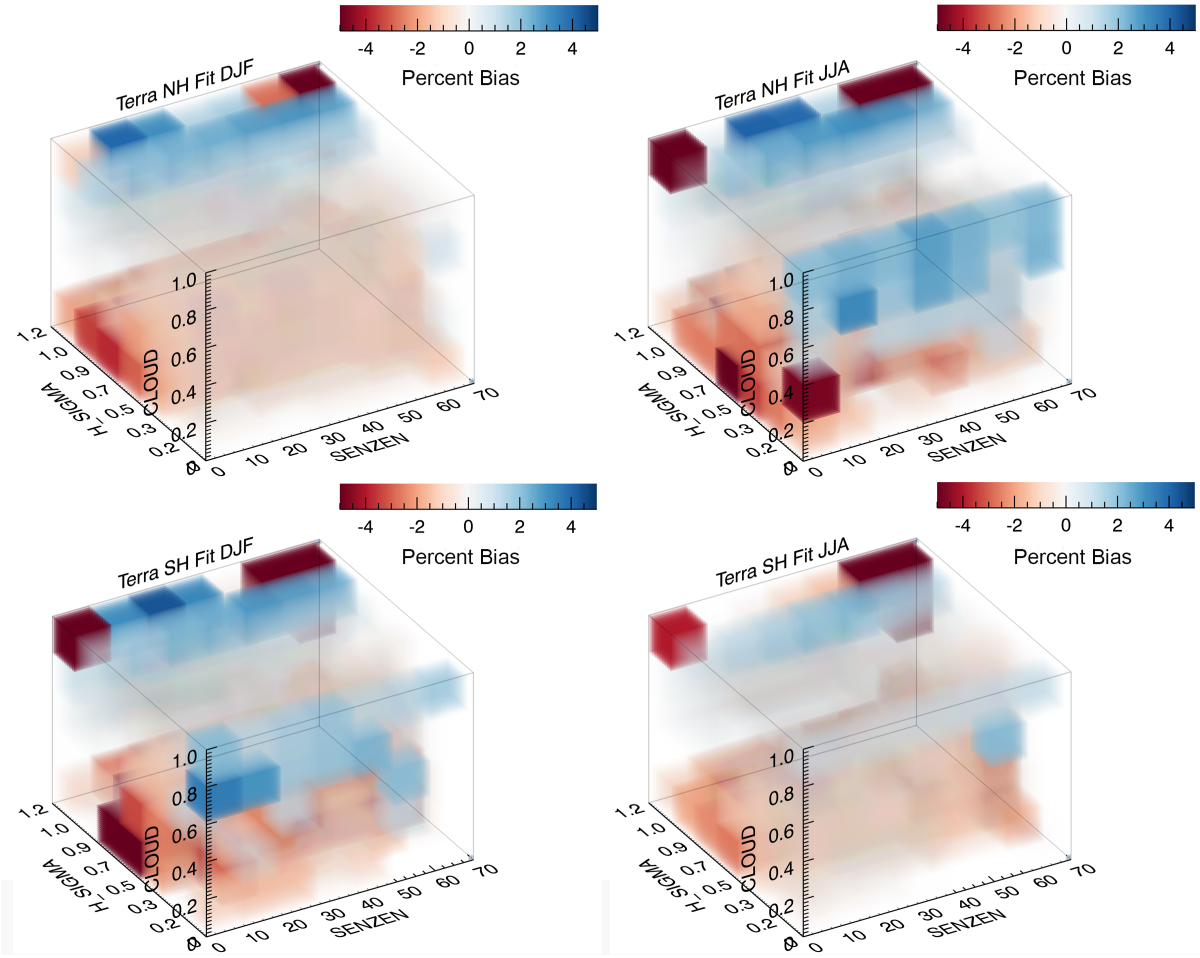

Figure 16. 3D histograms showing bias between fit derived reflectance and observed visible reflectance with respect to sensor zenith angle (x-axis), cloud heterogeneity (y-axis), and cloud fraction (z-axis) for Terra DJF (left) and JJA (right) in the northern (top) and southern (bottom) hemisphere

3.5.4 Discussion of Variable Sensitivities

The primary trend in the 3D histograms was the dependence on cloud fraction. For scenes with lower cloud fractions, there is an overall negative bias meaning the fit method is underestimating the observed visible reflectance. This would suggest that the distribution of LWP is skewed towards small values of liquid water path or the calculated cloud fraction of the scene is too small. At lower cloud fractions, there are fewer points available to calculate

the ideal coefficients for a fit function between the observed optical depth and corresponding visible reflectance, which may skew the LWP distributions.

With the incorporation of the cloud scene heterogeneity, it is possible to see how the scenes with higher cloud fraction tend to have a positive bias for certain cloud heterogeneities. Within the summer months for the northern and southern hemisphere, this was observed for both high cloud heterogeneity and low cloud heterogeneity. The winter months for the northern and southern hemisphere only showed the positive bias for high cloud heterogeneity. This means that scenes with overcast skies are overestimated by the fit method, which could imply that scenes with overcast skies may not benefit as heavily from using the fit method.

The effects of viewing geometry were primarily seen at scenes with lower cloud fractions, with a larger bias coinciding with angles closer to nadir. Many of the points closest to nadir were screened out due to the effect of sun glint over water, which makes it difficult to assess the success of the fit method for these angles.

Overall, there seemed to be minimal biases for scenes with midlevel cloud fractions between 0.2-0.8 along with heterogeneities varying from 0.2 to 1.0. These scenes did not show a large dependence on viewing angle. Though there are biases for certain scene scenarios, the fit method continually does better recreating the scene visible reflectance than the mask method.

3.6 Satellite Inter-comparison

An advantage of using this methodology is that it can be applied to any satellite dataset that provides measurements of visible reflectance and liquid water path, which allows for satellite comparison as well as applications of different cloud processing algorithms. In

this study, the method is applied to two different instruments, MODIS and AVHRR/NOAA-18, and two different types of cloud processing, standard MODIS processing with CSR and PATMOS-x. The main difference between the MODIS measurements and the PATMOS-x processed AVHRR/NOAA-18 and MODIS measurements is that PATMOS-x does not include any pixel filtering in the processing of cloud products. AVHRR/NOAA-18 has the closest equatorial overpass time to Aqua. The dataset for AVHRR/NOAA-18 contains data from 2005 to 2011 whereas the Aqua data is from 2003-2013.

Figure 17 and Figure 18 show the mean LWP using both the mask and the fit method for MODIS/Aqua, PATMOS-x/Aqua, and PATMOS-x/NOAA-18 along with the percent adjustment from the mask to the fit method for December to February and June to August. From December to February using the mask method, all three datasets show increased LWP in the northern hemisphere with PATMOS-x /AQUA possessing the largest values. PATMOS-x/NOAA-18 shows consistently lower values than both Aqua versions. The southern hemisphere mask LWP is softened using PATMOS-x in comparison to MODIS. For all three scenarios, the LWP values agree the most in the stratocumulus regions. As shown in section 3.3, the fit method decreases the mean LWP in comparison to the mask method since it's including the optically thin and edge pixels of clouds. PATMOS-x/AQUA remains the same showing the highest LWP values in comparison to PATMOS-x/NOAA-18 and MODIS/Aqua. To better visualize the difference between the fit and mask LWP, the percent adjustment is also plotted. MODIS/AQUA shows the largest adjustments globally. However, PATMOS-x/Aqua has the maximum adjustment in the northern hemisphere up to 45%. PATMOS-x/NOAA-18 shows the lowest amount of LWP adjustment especially in the southern hemisphere. The smallest adjustments for all three scenarios are in the

stratocumulus regions, suggesting that the cloud field is not in need of a large adjustment given the homogeneous landscape of these clouds.

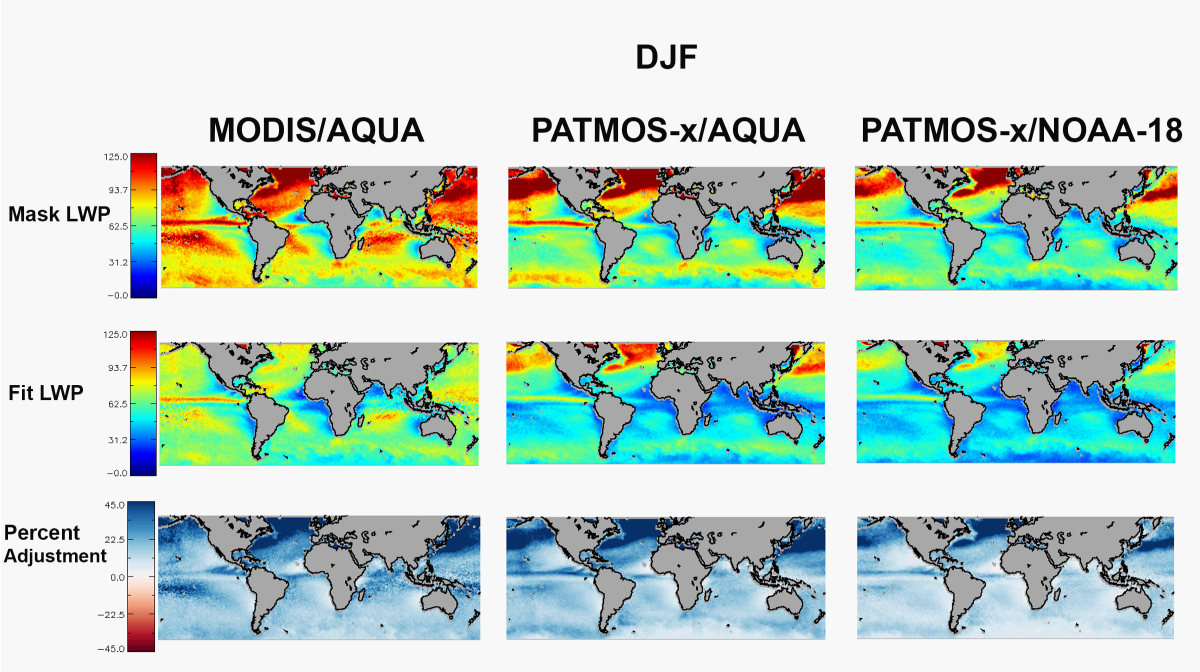

Figure 17. Satellite inter-comparison between MODIS/Aqua (left), PATMOS-x/Aqua (center), and PATMOS-x/NOAA-18 (right) displaying mean mask LWP (top), mean fit LWP (middle), and percent adjustment from the mask LWP to the fit LWP (bottom) from December to February. LWP is measured in units of g/m^2

For July to August, MODIS/Aqua displays the largest amount of LWP throughout the southern hemisphere, while PATMOS-x/Aqua and PATMOS-x/NOAA-18 show the greatest amount only along the southern hemisphere edge. Similar to the northern hemisphere winter, the fit method lessens the mean scene LWP. The percent adjustment from the mask LWP to the fit LWP continues to show the largest adjustment for MODIS/Aqua. PATMOS-x/Aqua also shows a large adjustment up to 45% along the edge of the southern hemisphere. Once again, PATMOS-x/NOAA-18 shows the smallest adjustment overall.

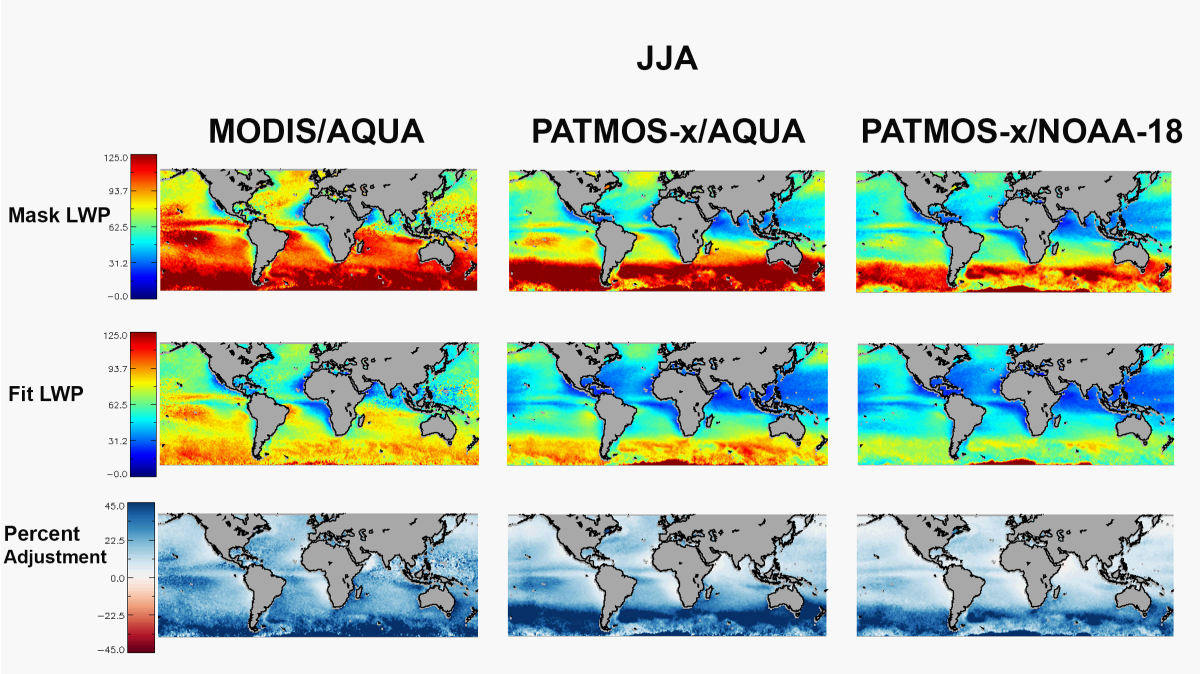

Figure 18. Satellite inter-comparison between MODIS/Aqua (left), PATMOS-x/Aqua (center), and PATMOS-x/NOAA-18 (right) displaying mean mask LWP (top), mean fit LWP (middle), and percent adjustment from the mask LWP to the fit LWP (bottom) from June to August. LWP is measured in units of g/m^2

With these LWP adjustments, the efficiency is determined by the ability to recreate the scene visible reflectance. Using the retrieved LWP according to the mask method for December to February, all of the scenarios over-estimate the scene visible reflectance (Figure 19). PATMOS-x/Aqua and PATMOS-x/NOAA-18 over-estimate the scene visible reflectance at a much smaller bias than MODIS/Aqua, especially in the northern hemisphere. Both PATMOS-x datasets shows a slight underestimation of the visible reflectance in the northern hemisphere associated with the highest amounts of LWP. When the fit method is applied, an opposite effect occurs with MODIS/Aqua showing the smallest bias and the larger biases from PATMOS-x/NOAA-18 and PATMOS-x/Aqua. All three scenarios primarily underestimate the scene visible reflectance. MODIS/Aqua shows slight overestimation in parts of the tropics. PATMOS-x/Aqua and PATMOS-x/NOAA-18 show

the largest underestimation in parts of the northern hemisphere, predominately in the northern portions of the Atlantic and Pacific oceans. From the percentage of improvement, MODIS/Aqua showed improvements over the entire area, while PATMOS-x/Aqua and PATMOS-x/NOAA-18 did not. Both showed improvement in the southern hemisphere and close to the equator in the northern hemisphere, but the fit method was not an improvement in the northern portion of the northern hemisphere around 60 degrees N. PATMOS-x/Aqua and PATMOS-x/NOAA-18 exhibit minor improvements in the stratocumulus regions over the North Pacific, South Pacific, and South Atlantic.

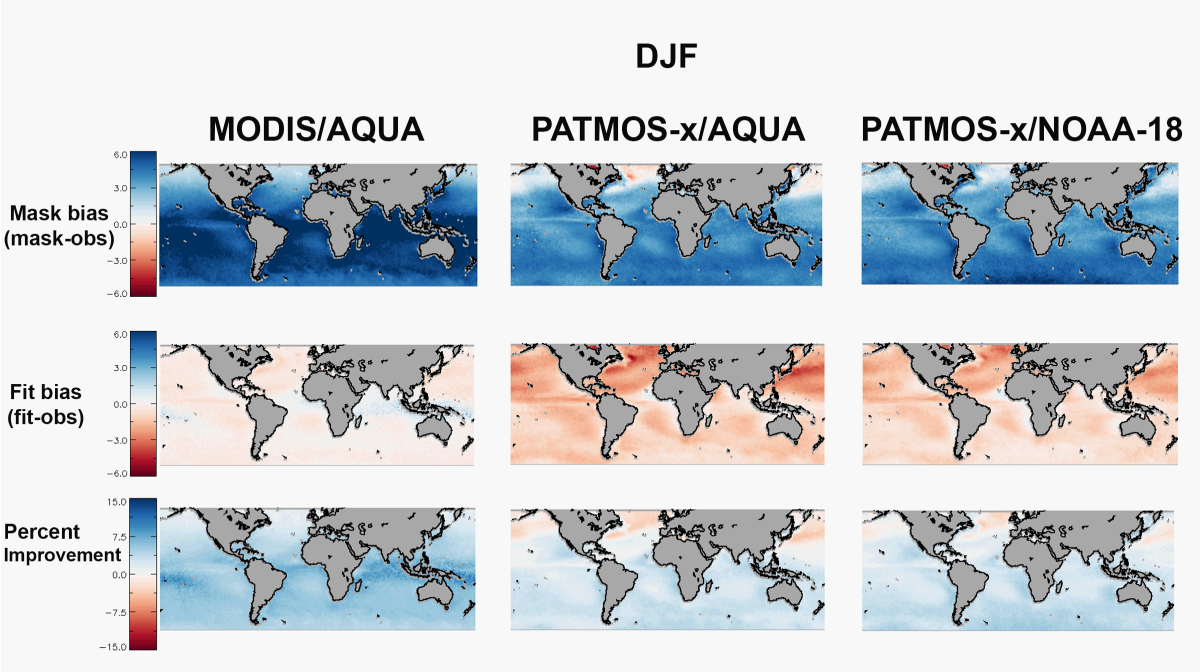

Figure 19. Satellite inter-comparison between MODIS/Aqua (left), PATMOS-x/Aqua (center), and PATMOS-x/NOAA-18 (right) displaying mean mask bias (top), mean fit bias (middle), and percent improvement from the mask method to the fit method (bottom) for December to February.

From June to August, the mask method shows overestimation for all three cases with the smallest biases occurring in the southern hemisphere (Figure 20). MODIS/Aqua displays strictly an overestimation throughout the ocean regions. PATMOS-x/NOAA-18 and

PATMOS-x/Aqua differ from MODIS/Aqua in that they show positive biases within the northern hemisphere and biases close to zero or slightly negative in the southern hemisphere. For MODIS/Aqua, the fit method recreates the scene visible reflectance with very small biases ranging from -2 to 2 with most of the ocean regions being skewed towards slight negative bias. For PATMOS-x/NOAA-18 and PATMOS-x/Aqua, there is a stronger negative bias in the southern hemisphere and slight positive bias along some of the ocean regions surrounding coastlines. Similar to the December to January cases, MODIS/Aqua shows improvements of using the fit method to recreate the scene visible reflectance over the oceans. PATMOS-x/NOAA-18 and PATMOS-x/Aqua show smaller improvements in the northern hemisphere and certain regions of the southern hemisphere, which did not improve with the application of the fit method.

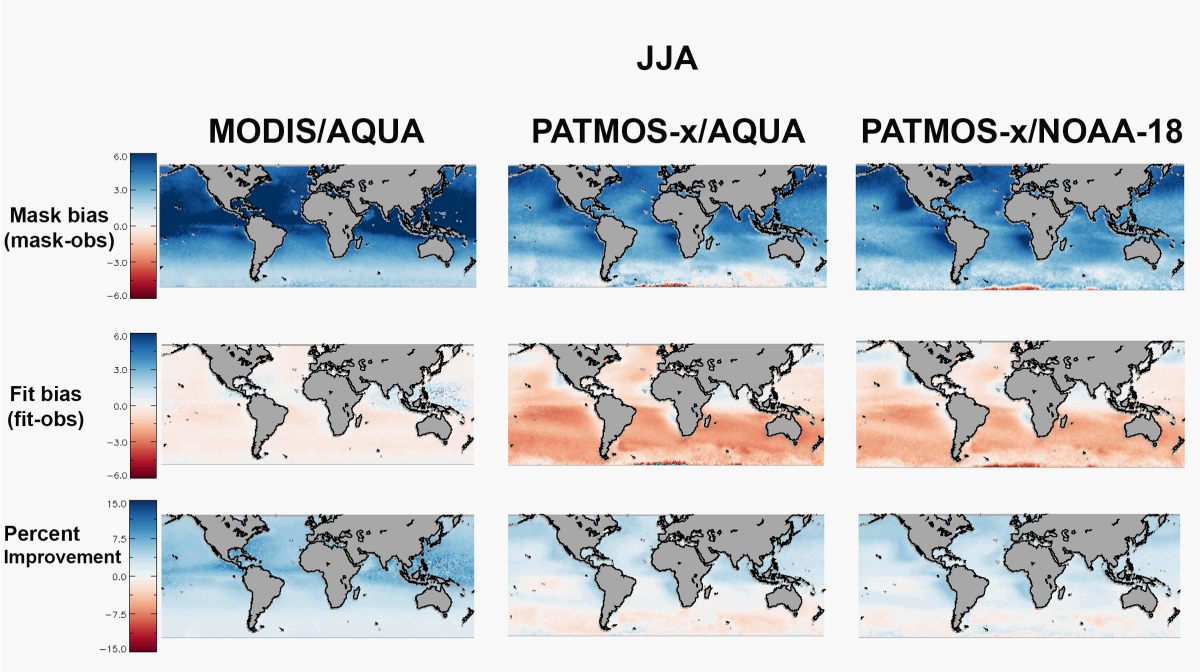

Figure 20. Satellite inter-comparison between MODIS/Aqua (left), PATMOS-x/Aqua (center), and PATMOS-x/NOAA-18 (right) displaying mean mask bias (top), mean fit bias (middle), and percent improvement from the mask method to the fit method (bottom) for June to August.

The application of the fit method continually recreates the scene visible reflectance better than the mask method for MODIS/Aqua, showing improvements over the ocean from 60 N to 60 S. Using PATMOS-x/Aqua and PATMOS-x/NOAA-18, benefits of using the fit method were only seen seasonally with improvements seen in the southern hemisphere during the boreal winter and in the northern hemisphere during the northern hemisphere summer. Certain areas also showed no improvement where the mask method was able to better recreate the scene visible reflectance than the fit method. This inter-comparison demonstrates how the fit method especially benefits methods that use pixel filtering to calculate cloud properties. Given that the PATMOS-x processing does not use pixel filtering for its cloud property retrievals, it did not experience the amount of improvement that the standard MODIS/Aqua data did. However, there are some cases where using the fit method would benefit PATMOS-x since there were a significant number of improvements in both the northern and southern hemisphere based on the season. The regions where the fit method did not excel for PATMOS-x/Aqua and PATMOS-x/NOAA-18 were the regions that experienced the largest adjustment in LWP from the mask method to the fit method. This suggests that the LWP could be underestimated from the fit method potentially causing these biases. The sources of these biases would have to be better explored for future studies.

4. External Heterogeneity

4.1 Introduction

The external heterogeneity is examined by using a spatial heterogeneity index and the incorporation of a 3D radiative transfer model. The spatial heterogeneity index was first introduced in section 3.5 with the 3D histograms to identify sensitivities to the fit methodology based on the cloud heterogeneity and viewing geometry. A 3D radiative transfer model is used to explore the resulting fluxes from the application of the fit method to account for internal heterogeneity and the spatial effects from using 1D radiative transfer in comparison to 3D radiative transfer. Given the computational resources required to run full 3D radiative transfer simulation over the entire globe, a 20 x 20 degree region over the North Pacific is subsetted to apply the model to (Figure 21). From a year of model data in 2010, an analysis is conducted using 3 different modeling scenarios including a 1D simulation using a scene averaged LWP from retrievals (Mask method), 3D simulation with the retrieved LWP (mask method) and 3D simulation using the derived LWP from the fit method.

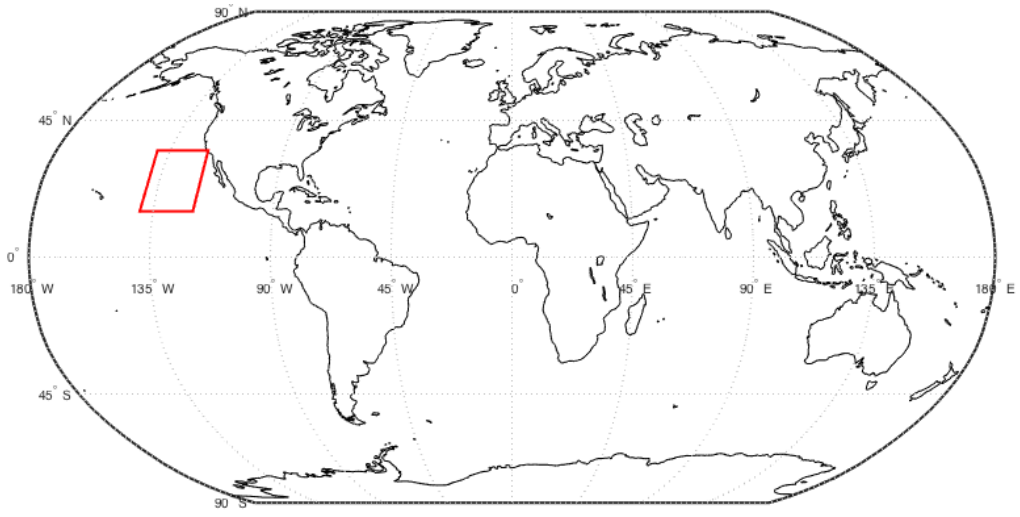

Figure 21. Global map highlighting North Pacific ocean region (red box) used for 3D radiative transfer model

4.2 Global Heterogeneity

The global heterogeneity is calculated by using the standard deviation of the scene visible reflectance divided by the mean scene visible reflectance over the 1 x 1 degree grid boxes (Liang et al., 2009) as seen in Equation 13.

$$H_\sigma = \frac{\sigma}{\overline{R}} \tag{13}$$

Lower values are indicative of homogeneous cloud scenes while higher values show more heterogeneous cloud scenes (Figure 22). For Aqua, the most heterogeneous clouds are seen around the tropics for all seasons. The magnitude of this heterogeneity in the tropics is the highest in June to August and the lowest in December to February. The lowest heterogeneity is located along subtropical western coasts lining up with the marine stratocumulus regions off the coasts of Angola, Peru and California. Terra shows very similar patterns to Aqua with very small changes in heterogeneity. Aqua shows a very slight increase in heterogeneity in comparison to Terra. These regions of high heterogeneity match very well with the areas of most improvement from the use of the fit method, especially along the tropics. This metric works best for comparing regions under the same solar zenith angle. At higher solar zenith angles, clouds are more likely to appear rougher or more heterogeneous from shadowing or illumination of cloud sides. At lower solar zenith angles, clouds may appear to be smoother due to horizontal transport of light (Girolamo et al. 2010).

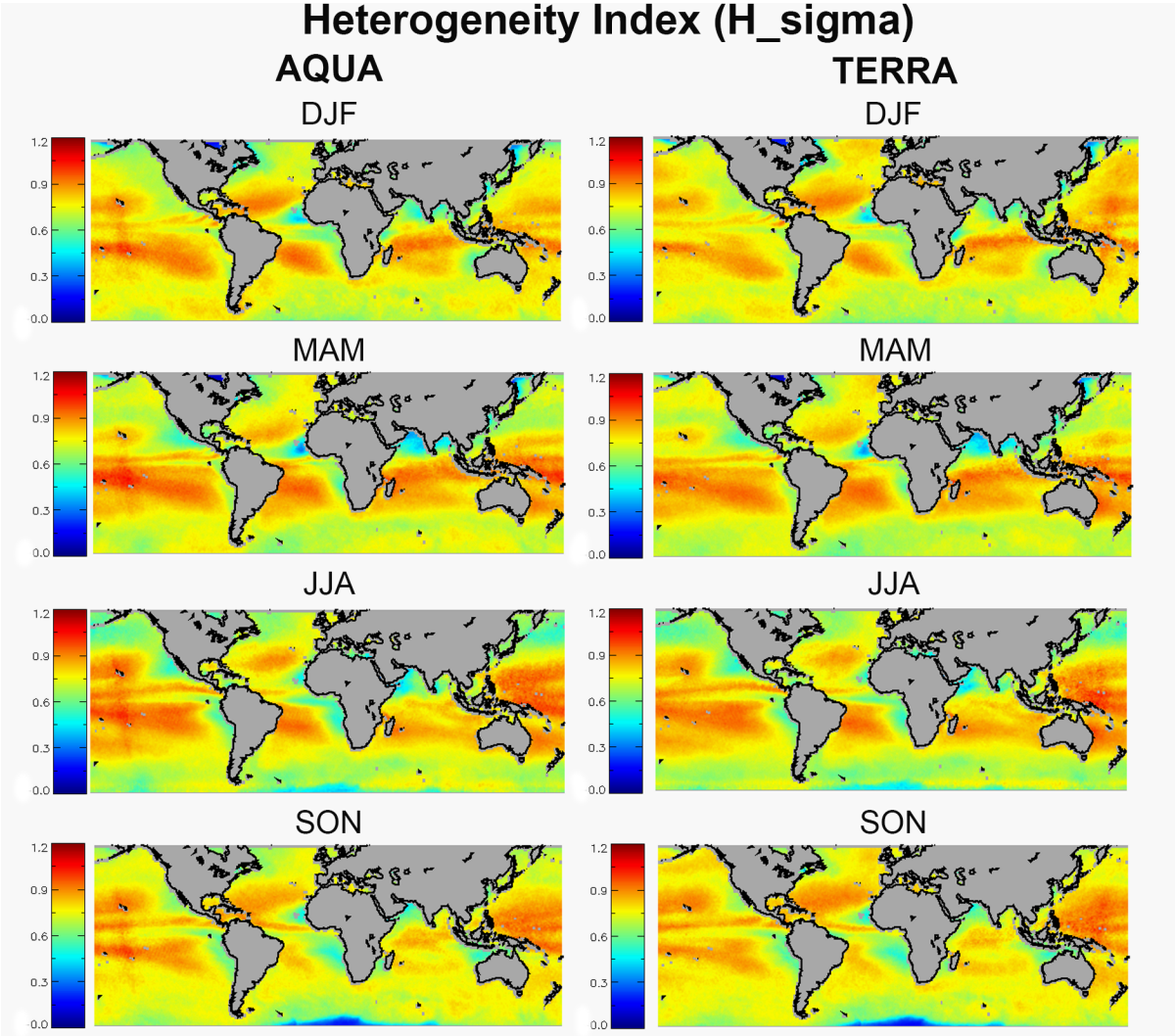

Figure 22. Seasonal heterogeneity index for Aqua (left) and Terra (right) from 2003-2013

4.3 Radiative Transfer Modeling

4.3.1 3D Mask vs. 1D Mask

As explained in Section 2.5, the 1D mask scene is calculated by using the mean cloud properties that were retrieved by MODIS and assigning it the MODIS cloud mask derived cloud fraction. The 3D mask scene is calculated from the 1km MODIS retrieved cloud properties over a 10 x 10 km grid. The solar flux is normalized to 1.0, so the output flux values can range from 0 to 1.0. An example of the differences in these scenes is shown in

Figure 23. In comparison to the 3D mask scene, the 1D mask lacks the cloud morphology along with horizontal distribution of cloud properties.

Beginning with the flux results, the top of the atmosphere (TOA) flux calculated from the 3D mask and the 1D mask scenes is compared seasonally. The gray X's represent the individual TOA flux for each scene. The black solid line is the mean 3D mask TOA flux binned according to the 1D mask TOA flux. For the most part, all seasons show a fairly strong 1:1 relationship between the 1D mask TOA flux and the 3D mask TOA flux. An interesting feature shown for all seasons is that the slope of the mean TOA flux line is decreased in comparison to the rest of the line for lower TOA flux values. This means that the 3D mask TOA flux is generally higher than the corresponding 1D mask TOA flux for values below 0.15 W/m^2. The lower flux values likely indicate a scene with a small amount of clouds with a heterogeneous field. This difference is possibly the result of the changes in the TOA flux from heterogeneous cloud compensating for the lack of cloud morphology within the 1D mask scenes.

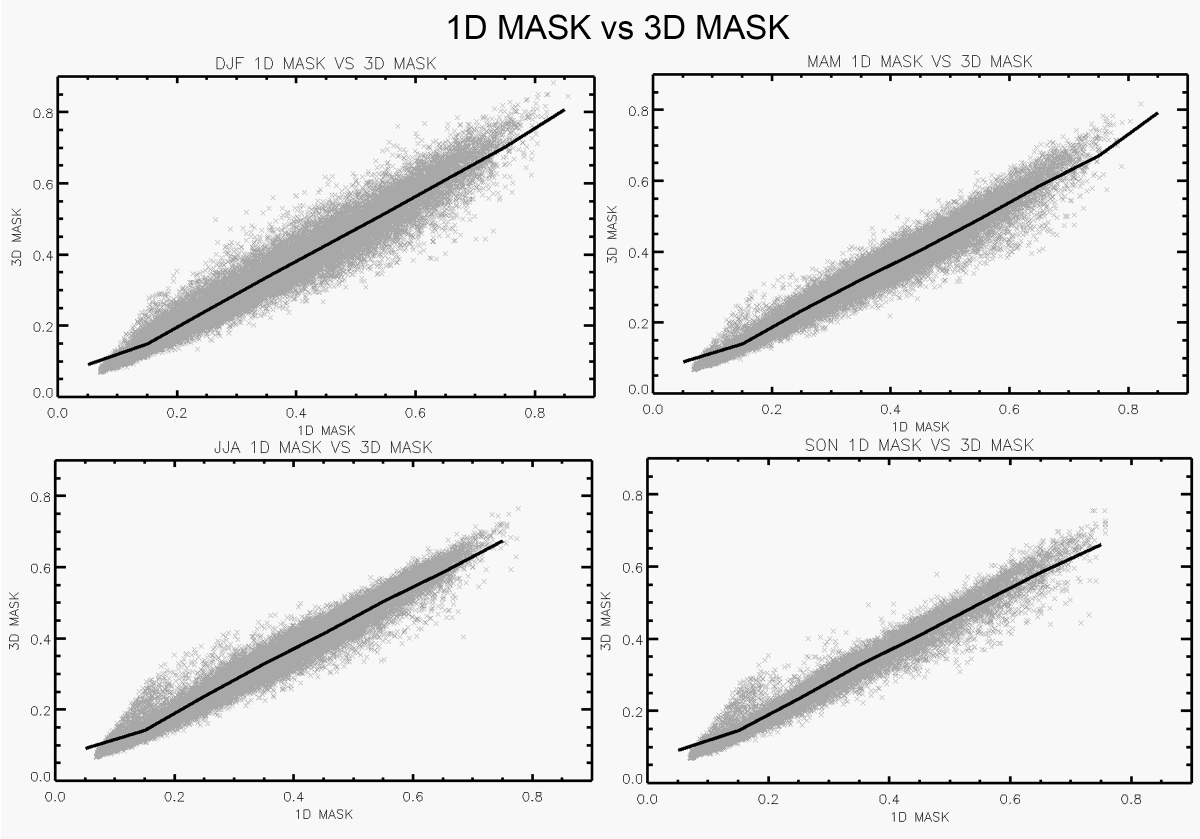

Figure 23. Scatter plot (gray) comparing normalized 1D mask TOA flux vs. 3D mask TOA flux seasonally over North Pacific for 2010 with mean 1D TOA Flux line (black)

To see if there are any dependencies on other contributing variables, the difference between the 3D mask TOA flux and the 1D mask TOA flux is compared to cloud fraction, viewing geometry, cloud heterogeneity, and visible reflectance. For cloud fraction, the small differences between the 3D mask TOA flux and 1D mask TOA flux does not show cloud fraction dependence for any of the seasons (Figure 24). For the points that do not hover around the zero mark, higher cloud fractions for DJF, MAM, and SON are more closely related to a negative difference in places where the 3D mask TOA flux is less than the 1D mask TOA flux, while JJA seems to have mid-level amounts of cloud fraction. The standard deviation of the TOA flux differences increases as the cloud fraction increases.

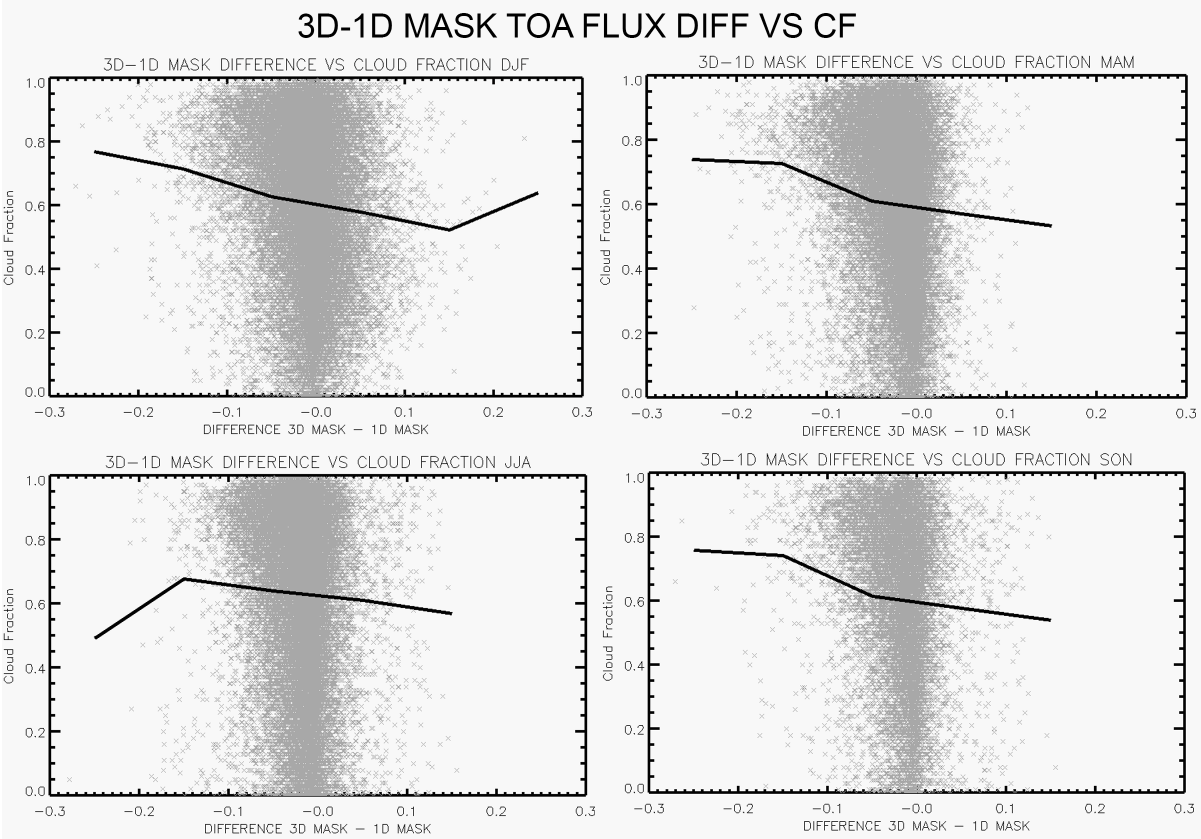

Figure 24. Scatterplot (gray) comparing difference between 3D mask and 1D mask TOA flux vs. cloud fraction seasonally over the North Pacific for 2010 with mean TOA difference line (black)

The cloud heterogeneity also has a concentration of points around zero in which the mean cloud heterogeneity is approximately 0.25 from December to May, and around 0.2 from June to November (Figure 25). The largest amount of cloud heterogeneity in the North Pacific region occurs in December to February, which corresponds to Figure 21 from the previous section. The distribution of the difference between the 3D mask and 1D mask TOA flux is skewed towards negative differences with the largest differences occurring around 0.2 W/m^2 for all seasons. The largest positive differences between the 3D mask TOA flux and the 1D mask TOA flux are associated with greater heterogeneities from June to November reaching a maximum mean of 0.3 and from December to May a slight decrease in the heterogeneity factor as the difference increases.

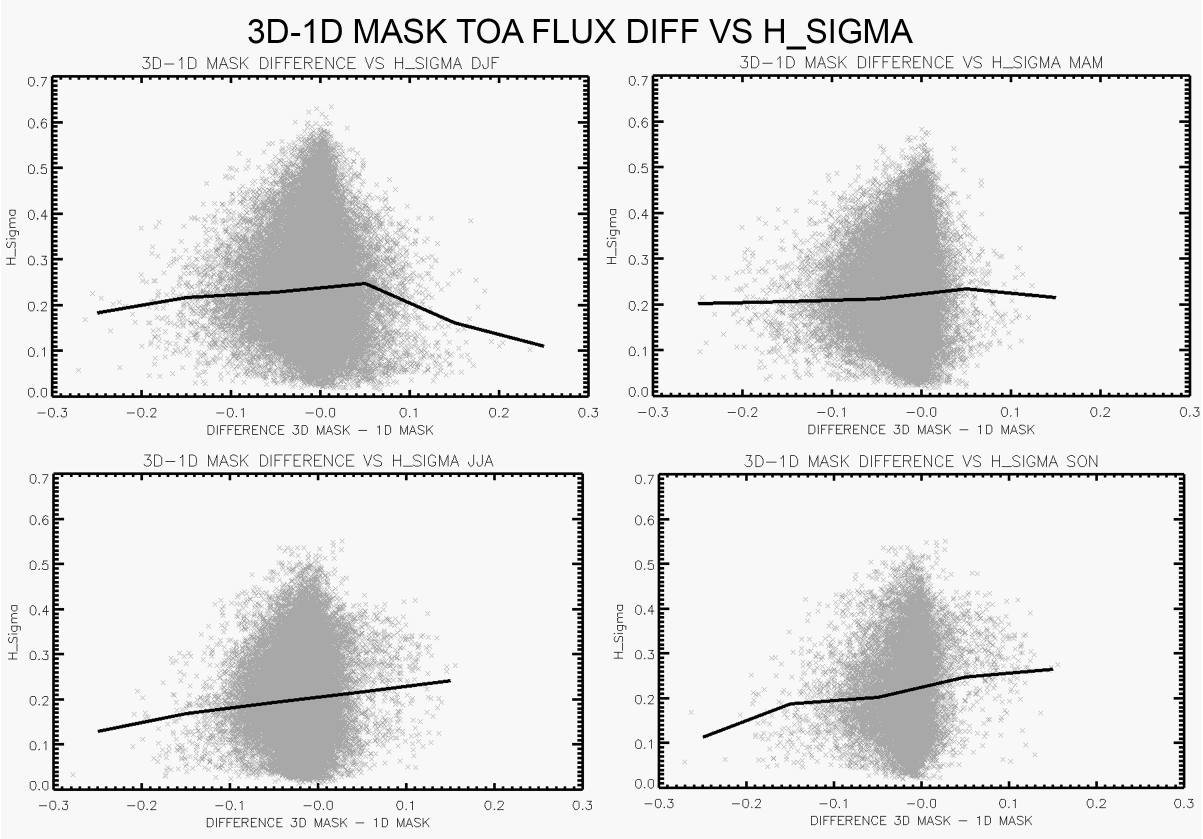

Figure 25. Scatterplot (gray) comparing difference between 3D mask and 1D mask TOA flux vs. heterogeneity index (H_sigma) seasonally over the North Pacific for 2010 with mean difference line (black)

For solar zenith angle for all seasons, the majority of the points are scattered around the center, indicating there were not many large changes between the 3D and 1D TOA flux (Figure 26). December to February show the largest range of solar zenith angles, with higher solar zenith angle being associated with positive differences between the 3D mask and 1D mask TOA flux, and mid range solar zenith angle from 35 to 45 degrees being more likely to have a negative difference between the 3D mask and 1D mask TOA flux. The other seasons show a smaller range of solar zenith angles with no significant dependence on the solar zenith angle.

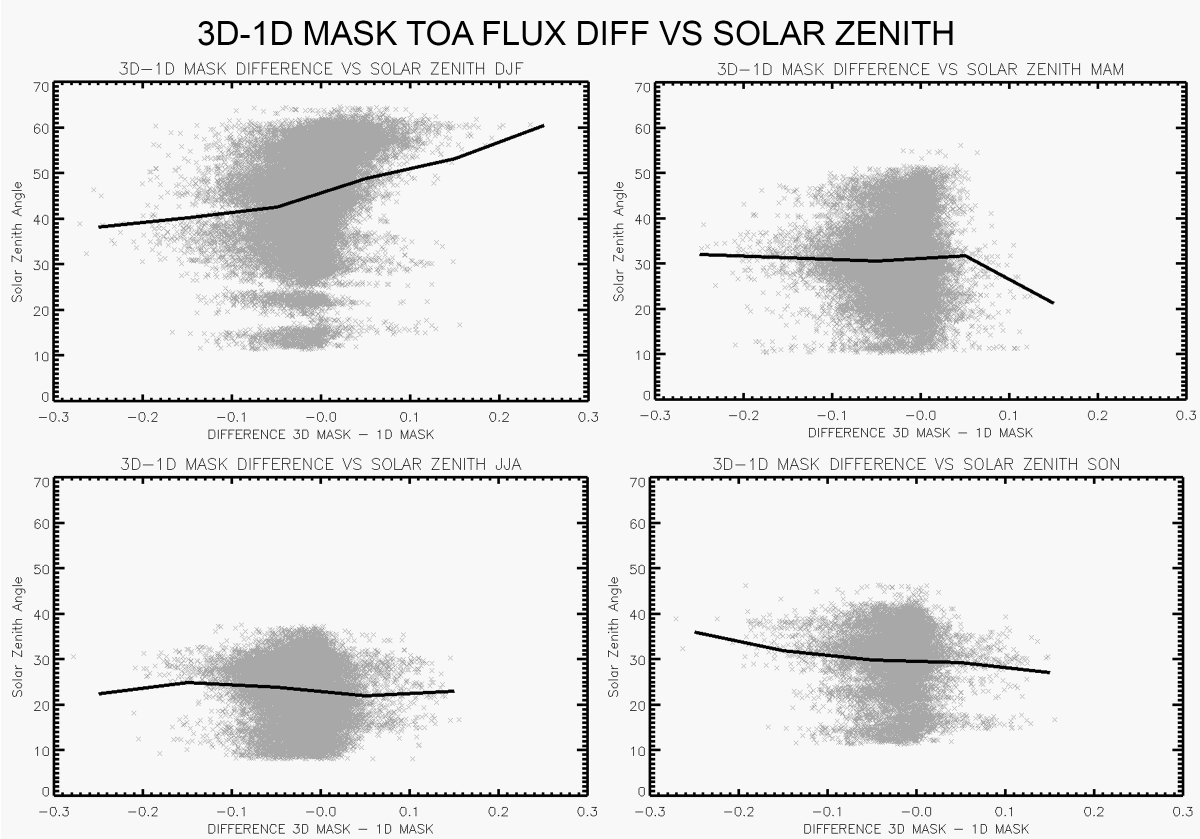

Figure 26. Scatterplot (gray) comparing difference between 3D mask and 1D mask TOA flux vs. solar zenith angle seasonally over the North Pacific for 2010 with mean difference line (black)

Sensor zenith angle does not show much of a seasonal pattern for the differences between the 3D mask and 1D mask (Figure 27). Many of the points are scattered along the zero line, though as the sensor zenith angle increases, the range of differences begins to also increase in both the positive and negative directions. This suggests that the further the sensor zenith angle is from nadir, the more the 1D plane parallel assumption does not accurately reflect a truly 3D scenario.

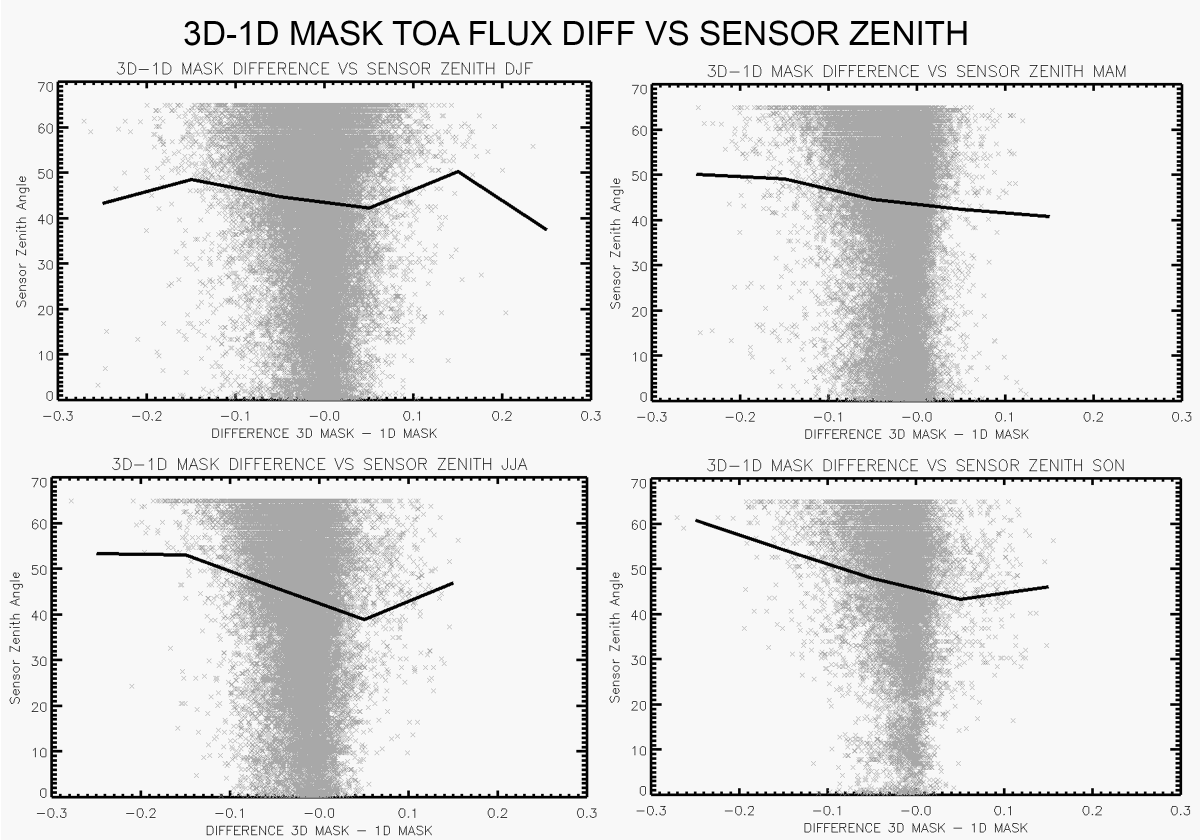

Figure 27. Scatterplot (gray) comparing difference between 3D mask and 1D mask TOA flux vs. sensor zenith angle seasonally over the North Pacific for 2010 with mean difference line (black)

Overall, there are not very significant dependencies on viewing geometry, cloud heterogeneity, or cloud fraction. This is likely due to the fact that there were not very large differences detected between the 3D mask TOA flux and the 1D mask TOA flux. Most notable detection of the differences between the 3D mask and 1D mask TOA flux were seen for mid range cloud heterogeneity and high sensor zenith angles. These differences were likely caused by the spatial arrangement of the cloud field and the cloud shadowing and illumination due to the high viewing angle.

Finally, the mean scene visible reflectance over the 10 x 10 km scene is compared to the mean TOA flux. The TOA flux can be compared to the visible reflectance given their similarity in magnitude to one another in the visible spectrum. The better the correlation is

between the mean scene visible reflectance and the mean TOA flux, the more representative the scene is of both the optical properties and radiative effects. Comparing the 1D mask TOA fluxes to the scene visible reflectance, there is a decent fit between the two variables (Figure 28). Seasonally, the 1D mask TOA fluxes contain a greater amount of outliers from December to February, while the least amount of outliers is from June to August. For all the seasons, the 1D mask TOA flux is consistently lower than the visible reflectance when comparing them to a 1:1 ratio. The 1D mask TOA flux shows the lowest amount of correlation from December to February and the highest amount of correlation from June to August. The North Pacific Ocean region is less heterogeneous in the summer months than the winter months, which could explain the better correlations between the TOA flux and visible reflectance in the summer.

The 3D mask TOA flux also shows a similar relationship with the visible reflectance, with the largest correlation seen from June to August and the lowest correlation occurring from December to February (Figure 29). From December to February, the correlation between the TOA flux and visible reflectance is very similar for both the 1D mask and 3D mask. The main difference between the 1D mask and 3D mask is seen from June to August. The relationship between the TOA flux and visible reflectance is much stronger using the 3D mask scenario in comparison to the 1D mask scenario. Although there are only small differences between the 1D mask and 3D mask radiative transfer simulations, the use of the 3D mask that includes the horizontal distribution of LWC and cloud morphology shows a better representation of the radiative field.

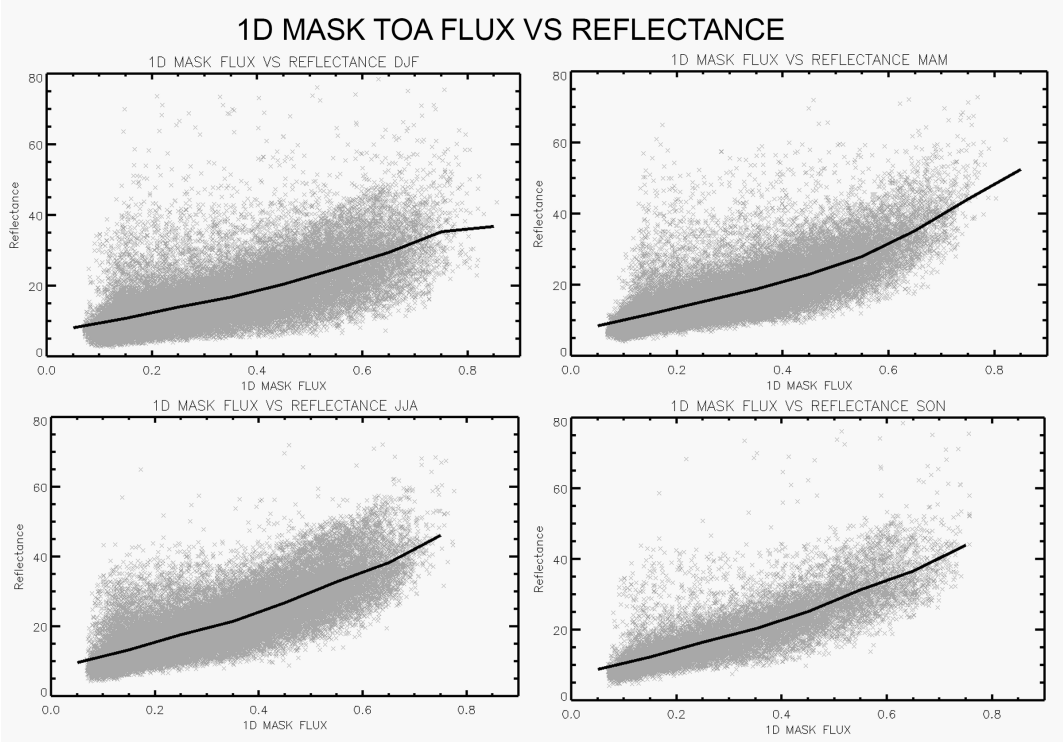

Figure 28. Scatterplot (gray) comparing difference between 1D mask TOA flux vs. visible reflectance seasonally over the North Pacific for 2010 with mean TOA flux line (black)

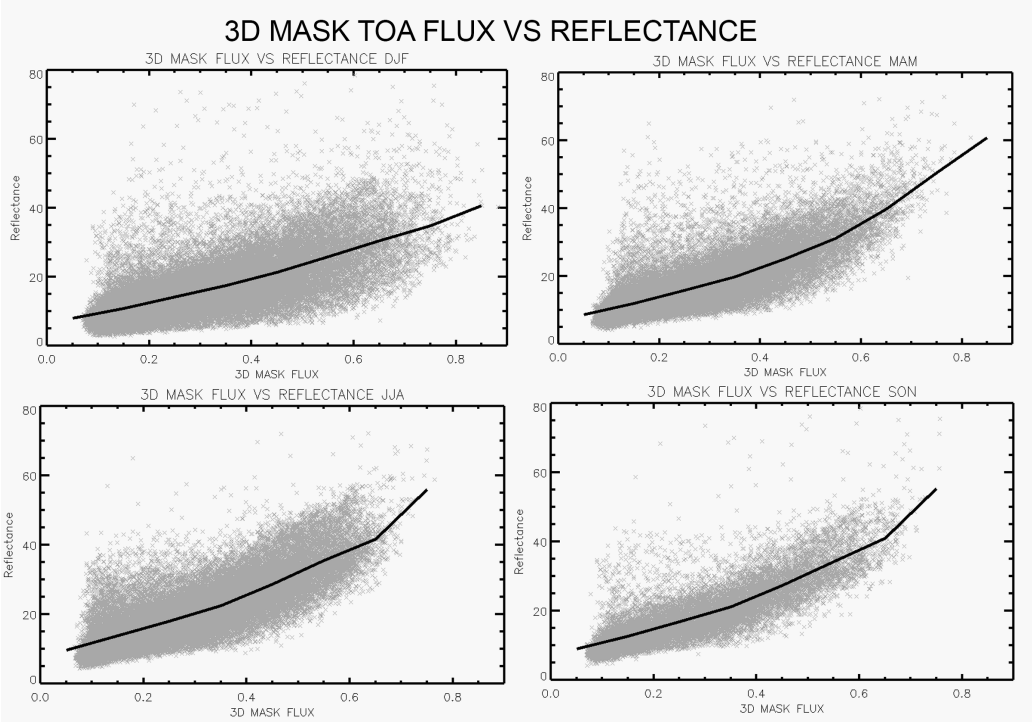

Figure 29. Scatterplot (gray) comparing difference between 3D mask TOA flux vs. visible reflectance seasonally over the North Pacific for 2010 with mean TOA flux line (black)

4.3.2 3D Mask vs. 3D Fit

From comparing the 3D mask and 1D mask TOA fluxes, the radiative differences between the two scenarios show the value of representing cloud morphology and the horizontal distribution of cloud properties in radiative transfer modeling. The next issue to investigate is the effect of skewed distributions of cloud properties on radiative transfer due to pixel filtering methods. The 3D fit TOA fluxes were derived from the fit methodology to compute the horizontal distribution of LWP.

When comparing the initial 3D TOA fluxes seasonally to each other, the 3D fit method shows overall lower TOA flux values than the 3D mask method (Figure 30). For lower TOA flux values, there are smaller differences between the mask and fit method, while for higher TOA fluxes there's a larger range of differences. This observation is consistent for all seasons. The 3D fit TOA flux likely shows lower values than the 3D mask TOA flux due to the adjustment of the LWP, which are adjusted to smaller values to incorporate edge pixels or optically thin clouds.

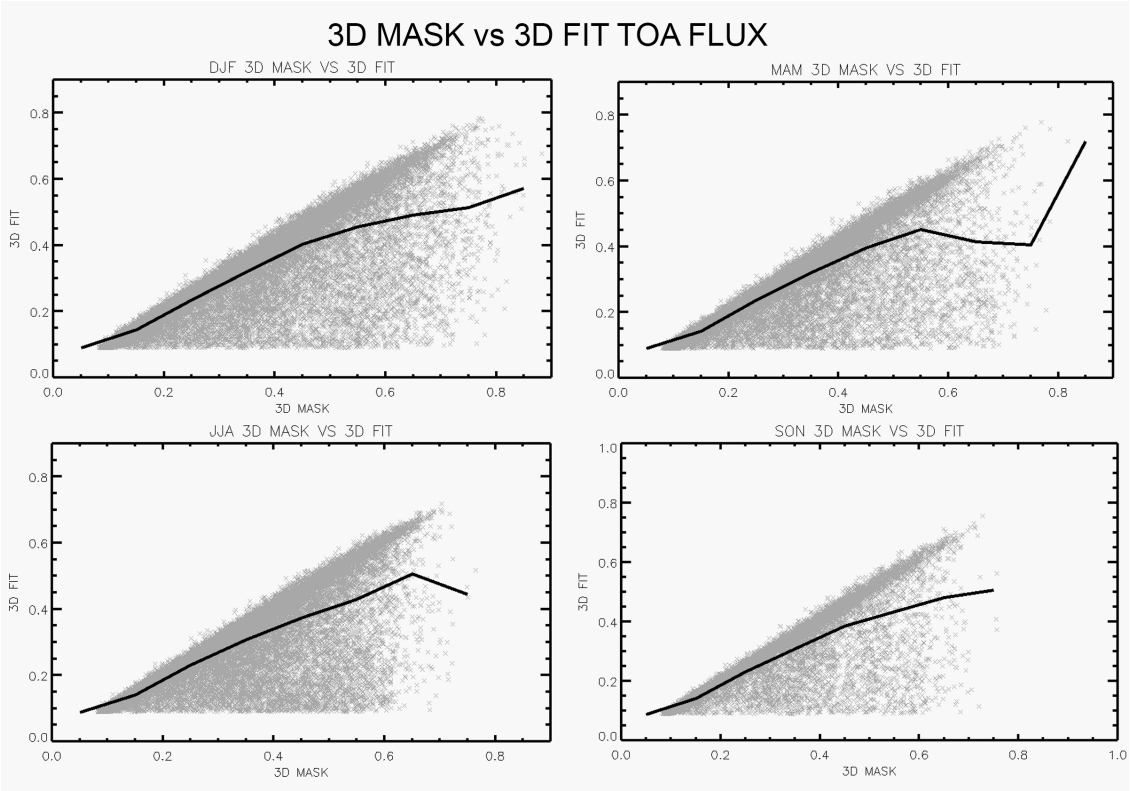

Figure 30. Scatter plot (gray) comparing normalized 3D mask TOA flux vs. 3D fit TOA flux seasonally over North Pacific for 2010 with mean 3D TOA flux line (black)

To see if these differences between the 3D fit and 3D mask TOA fluxes are affected by variables which often have an impact on full 3D radiative transfer, the differences are compared to cloud fraction, cloud heterogeneity, and viewing geometry. For all seasons, the largest differences are seen at the lowest cloud fractions (Figure 31). The differences between the 3D fit and 3D mask TOA flux steadily increase to zero as the cloud fraction increases. For scenes with higher amounts of cloud fraction, the fit method has more retrieval of cloud properties to create a stronger fit function between the optical retrievals and observed visible reflectance. This is likely the cause of the minimal differences seen at cloud fractions above 0.8 for all seasons.

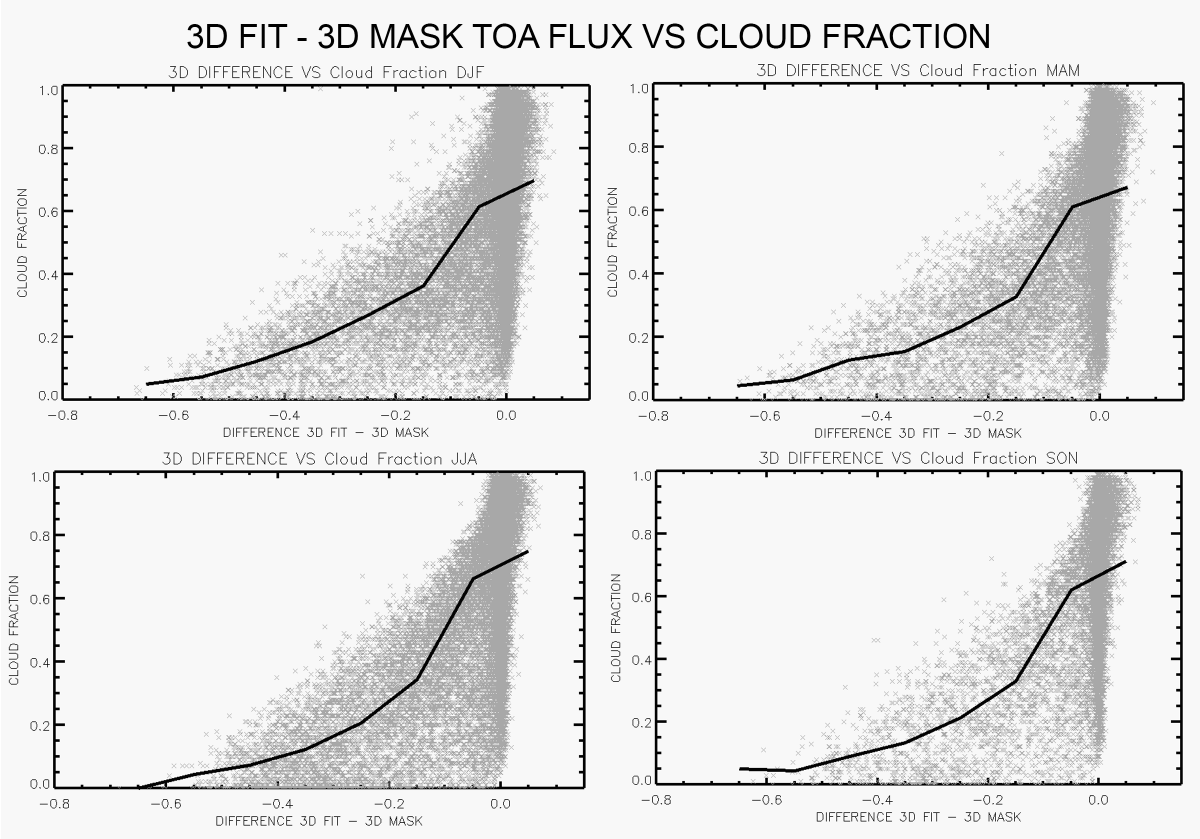

Figure 31. Scatterplot (gray) comparing difference between 3D fit and 3D mask TOA flux vs. cloud fraction seasonally over the North Pacific for 2010 with mean difference line (black)

The cloud heterogeneity in comparison to the differences between the 3D fit and 3D mask TOA flux shows an interesting relationship (Figure 32). The largest difference between the 3D fit and 3D mask TOA flux is observed when the cloud heterogeneity index is the lowest, indicating homogeneous clouds. This association could possibly be due to the fact that the fit method provides the largest amount of improvement for heterogeneous cloud scenes, so these some of differences in the TOA flux could likely be attributed to the fit method performance rather than the effects of pixel filtering. For cloud heterogeneity index values above 0.1, these are indicators of heterogeneous cloud scenes, with scenes becoming more heterogeneous as the value increases. There are no highly heterogeneous scenes (heterogeneity index values above ~0.8) observed. This is likely due to the structure of

stratocumulus clouds typically seen in the North Pacific Ocean region selected. Though there are differences seen for cloud heterogeneity values between 0.2 to 0.5, which could either be attributed to the adjustment of the scene LWP for more realistic radiative transfer or the fit method being unable to recreate the scene visible reflectance due to being more homogeneous in nature. More research would need to be performed to separate the errors from when the fit method performs poorly in order to quantify the effects of skewed horizontal distributions of cloud properties.

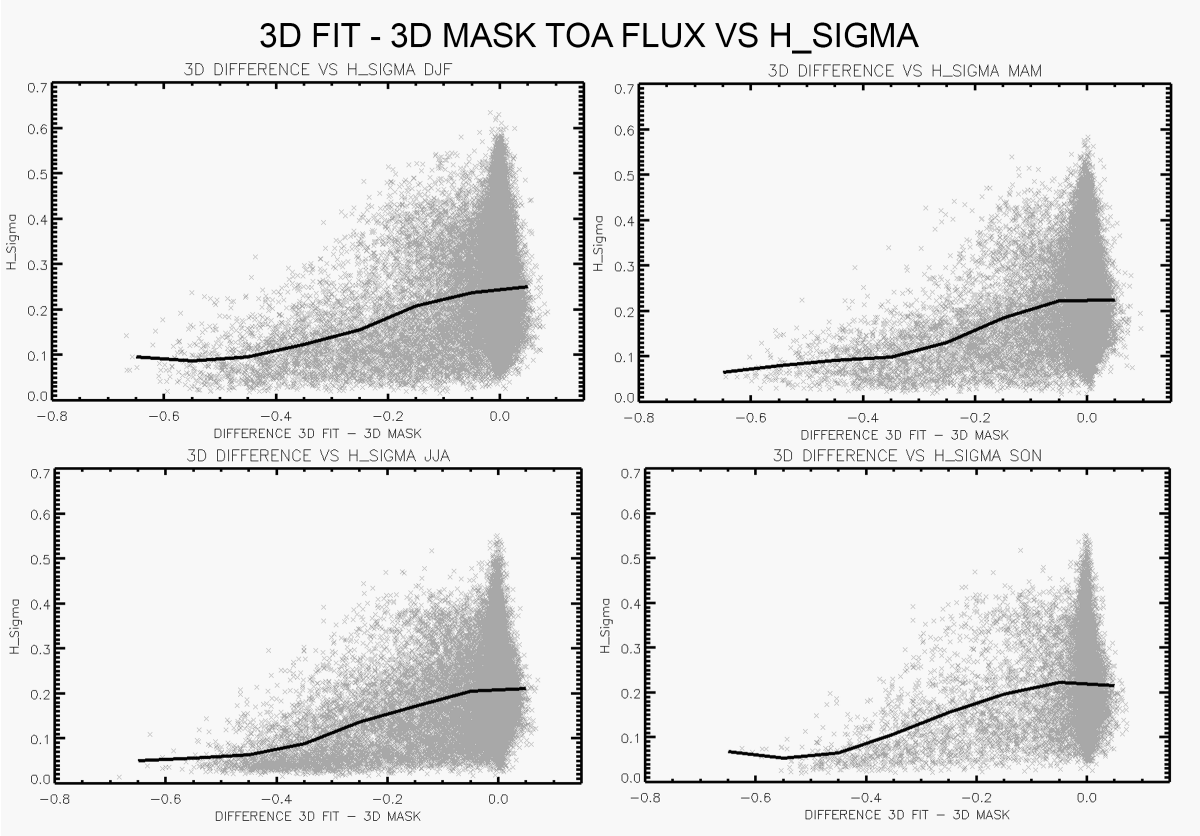

Figure 32. Scatterplot (gray) comparing difference between 3D fit and 3D mask TOA flux vs. heterogeneity index (H_sigma) seasonally over the North Pacific for 2010 with mean difference line (black)

The range of the solar zenith angles differs based on the seasons (Figure 33). For TOA flux differences close to zero, the distribution of solar zenith angles is fairly even along

its range of angles for each season. The greatest concentration of differences between the 3D fit and 3D mask TOA flux for each season are located around their maximum observed solar zenith angle. The clouds located at higher solar zenith angles are more likely to experience the effects of cloud illumination or cloud shadowing which could easily change the scene radiative effects when the cloud scene morphology is altered.

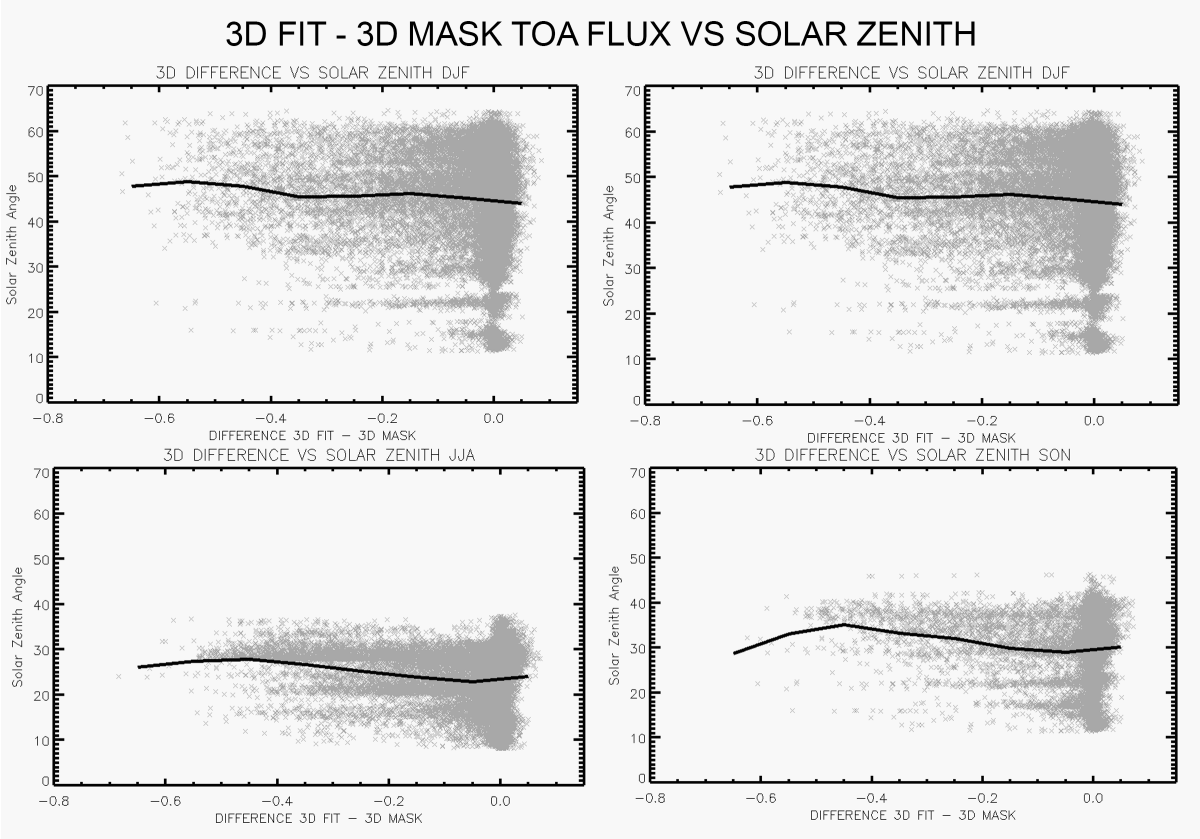

Figure 33. Scatterplot (gray) comparing difference between 3D fit and 3D mask TOA flux vs. solar zenith angle seasonally over the North Pacific for 2010 with mean difference line (black)

Sensor zenith angle also shows a similar effect with a large portion of the TOA fluxes distributed evenly along differences close to zero (Figure 34). However as the sensor zenith angle increases, the concentration of TOA flux differences close to zero begins to spread out towards negative differences between the 3D fit and 3D mask TOA fluxes. For TOA flux differences from -0.4 to -0.5 W/m^2, the mean sensor zenith angle peaks for all seasons. Past -

0.5 W/m^2, the sensor zenith angle slightly decreases. Higher sensor zenith angles are likely more susceptible to these differences due to being along the edge of scan, which leaves cloud retrievals likely to be exposed to the effects of cloud shadowing and cloud illumination.

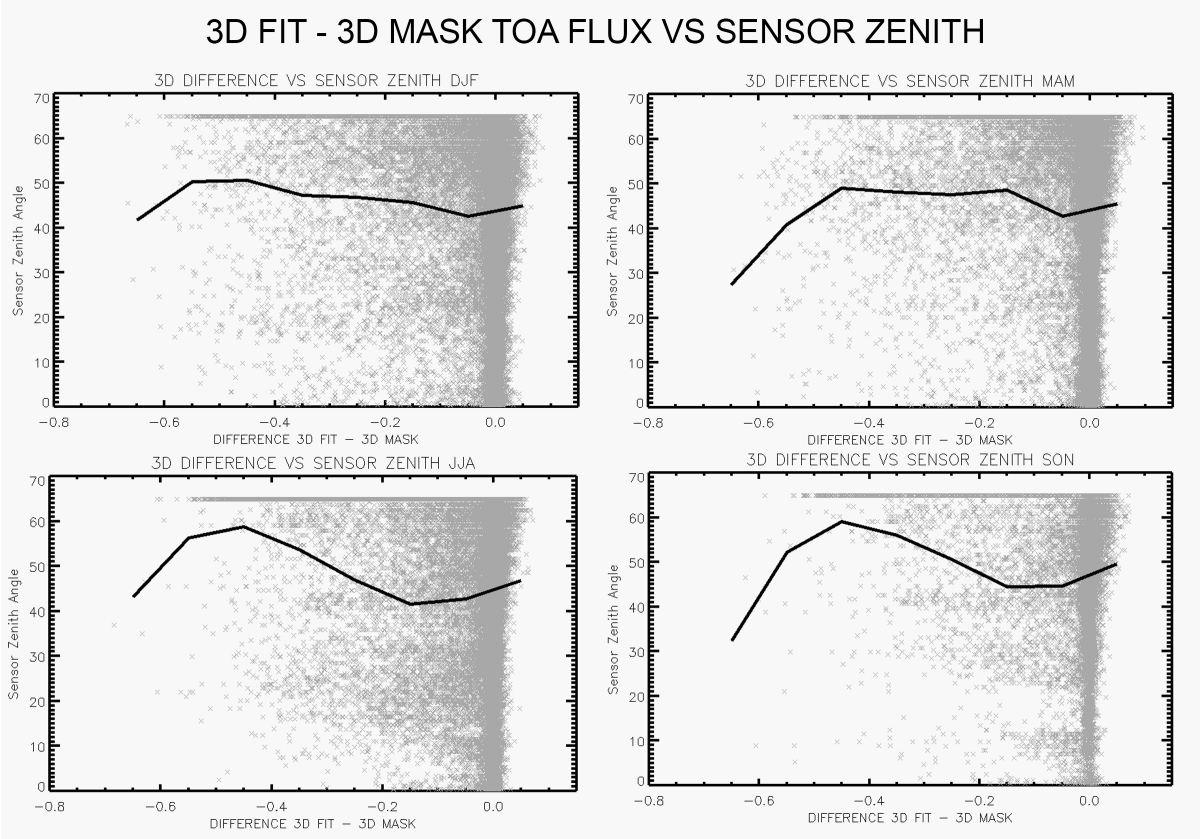

Figure 34. Scatterplot (gray) comparing difference between 3D fit and 3D mask TOA flux vs. sensor zenith angle seasonally over the North Pacific for 2010 with mean difference line (black)

As mentioned in section 4.3.1, the 3D mask TOA flux is better correlated with the observed visible reflectance in June to August than December to February. When the 3D fit TOA fluxes are compared to the observed visible reflectance, the correlation is also better for June to August than December to February as seen in Figure 35. Overall, the 3D fit TOA flux shows a larger range of values for lower values of visible reflectance suggesting that the fit method does better for mid range to higher reflectance values. When comparing the 3D fit and 3D mask to the visible reflectance, it is clear that the 3D mask is better matched with the

visible reflectance at lower flux values than the 3D fit for all seasons. Both show the best correlation for higher flux values from June to August. For December to February, the 3D mask method performed better overall than the 3D fit method. The application of the 3D fit and 3D mask method for 3D radiative transfer has only been applied to a generally homogeneous stratocumulus region in the North Pacific, which is a region that experiences a smaller amount of improvement from using the fit method over the mask method in comparison to other regions studied. The benefits of the fit method are more likely to be experienced in a more heterogeneous cloud regime. Section 6 will describe the future work that will be done to quantify the impacts of 3D radiative transfer due to the effects of skewed cloud property distributions from MODIS.

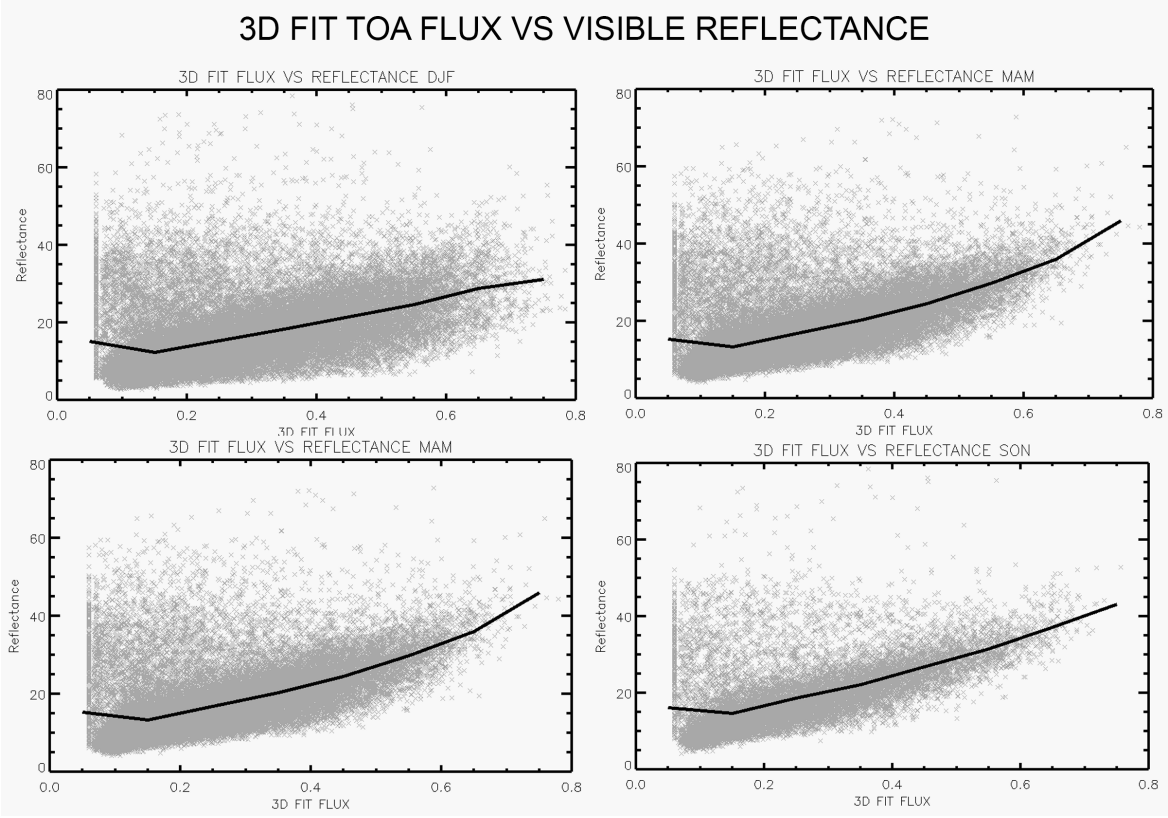

Figure 35. Scatterplot (gray) comparing difference between 3D fit TOA flux vs. visible reflectance seasonally over the North Pacific for 2010 with mean TOA flux line (black)

5. Conclusions

The effects of internal heterogeneity were explored by the application of the fit method used to create horizontal distributions of cloud properties over a 1 degree x 1 degree area and were assessed by how well the method could recreate the observed scene visible reflectance using the MODIS instrument both on Aqua and Terra from 2003-2013. The fit method adjusted the mean LWP based on a fit function between retrieved optical depth and the visible reflectance and applied this function to the entire scene of measurements in an effort to restore pixels without retrievals that could possibly be cloud edges or optically thin. The largest adjustments of the mean LWP from the fit method were observed to be seasonal with the Northern hemisphere showing the largest adjustments from December to February and the Southern hemisphere showing the largest adjustment from June to July. When the mask method was used to recreate the scene visible reflectance, the mask method continually overestimated the scene visible reflectance. The mask method also showed a seasonal cycle in the magnitude of its overestimation with the largest overestimation occurring in the northern hemisphere from June to August and in the southern hemisphere from December to February. Generally, the fit method tended to slightly underestimate the observed visible reflectance, but the magnitude of this underestimation was much lower than the mask method. Slight overestimation of the visible reflectance with the fit method occurred in the tropics. Monthly averages of the bias between the fit derived reflectance and the observed visible reflectance showed very little to no bias for all months. The amount of improvement of utilizing the fit method over the mask method showed global improvement when the fit method was used. Areas in the tropics improved up to 15%. The stratocumulus regions off

the coast of California, Peru, and Angola were notable areas where the least amount of improvement occurred likely due to their homogeneous structure.

Given that the fit method showed slight biases for underestimating and overestimating in certain areas, 3D histograms were used to determine sensitivities of the fit method with respect to cloud fraction, cloud heterogeneity, and viewing geometry. A negative bias or underestimation of the visible reflectance was seen in scenes with low cloud fraction, which was likely due to the lower amount of optical retrievals used to calculate an optimal fit function. Cloud heterogeneity showed the largest effect on high cloud fractions. In both the northern and southern hemisphere summer months, there was a positive bias for both high and low values of the cloud heterogeneity index, while the winter months for both hemispheres showed only a positive bias for high cloud heterogeneity values. The effects of viewing geometries showed a negative bias for low cloud fraction increasing in magnitude as the angles become closer to nadir. The fit method did not show much sensitivity to scenes with medium amounts of cloud fraction and mid-value cloud heterogeneity index, which means the application of the fit method would most help these scenes.

A satellite inter-comparison was also conducted since the fit method can be applied to any dataset that contains both cloud property retrievals and visible reflectance measurements. The PATMOS-x processing was used on both Aqua and NOAA-18, which unlike MODIS does not base its retrieval algorithms on pixel filtering processes. Overall, MODIS/Aqua showed the most improvement from using the fit method over the mask method. Both PATMOS-x/Aqua and PATMOS-x/NOAA-18 showed improvements with using the fit method in each hemisphere's respective summer months. Surprisingly, the mask method did better in the hemispheric winter months for both PATMOS-x/NOAA-18 and PATMOS-

x/Aqua. The areas where the fit method did not improve the recreation of the scene visible reflectance were associated with the largest reduction in LWP due to the fit method adjustment. This suggests that perhaps these areas were not in need of adjusting the mean scene LWP since they already potentially included the pixels that MODIS/Aqua had filtered out.

The external heterogeneity was analyzed by spatially viewing the cloud heterogeneity index and the use of a 3D radiative transfer model where the adjustments to account for the horizontal distribution of cloud properties and cloud morphology are compared using three scenarios. The most heterogeneous clouds are located along the tropics, which coincides with where the fit methodology shows the most improvement. The areas that show the least amount of heterogeneity correspond with the stratocumulus regions that have already been noted.

The 3D radiative transfer model was utilized over a stratocumulus region in the North Pacific Ocean for the year 2010. The three scenarios used were the 1D mask derived plane parallel, the 3D mask derived, and the 3D fit derived. The comparison between the 1D mask and 3D mask showed the differences in the TOA fluxes when cloud morphology is included. There changes in the TOA fluxes between the 3D mask and 1D mask scenarios were small, but overall there was a better correlation between the 3D mask TOA flux and the visible reflectance than the 1D mask TOA flux and the visible reflectance. The largest differences between the 3D mask and 1D mask TOA fluxes were for higher cloud fraction values, mid-range cloud heterogeneity, and viewing geometry further from nadir. The 3D mask and 3D fit were compared to show the differences between TOA fluxes when the horizontal distribution of cloud properties is altered to include pixels that were potentially filtered out by the CSR

algorithm. The 3D fit TOA flux was not very well correlated with the lower visible reflectance values in comparison to the 3D mask TOA flux. The 3D mask and 3D fit TOA fluxes were both decently well correlated with high visible reflectance, especially during the northern hemisphere summer. The largest TOA flux differences were observed at low cloud fraction, low cloud heterogeneity, and higher viewing geometry.

Overall, the stratocumulus region chosen is not known for having heterogeneous clouds, so the fit method might not be providing the same amount of improvement as seen in highly heterogeneous regions. It is therefore hard at this point to fully assess the radiative impact with the application of the fit methodology. Future work will include a more thorough analysis of these radiative effects.

6. Future Work

Much of the future work on this study will expand upon the 3D radiative transfer aspect. More model runs will be performed over the MODIS record to correspond to the application of the fit method, which extended from 2003-2013 for both Aqua and Terra. A few more ocean areas will also be included in the model to incorporate more of the marine stratocumulus regions as well as selecting a few cloud heterogeneous ocean regions. In addition to comparing the TOA fluxes from the model to the observed visible reflectance, the TOA radiances will be computed to enable a better comparison to assess how well both the fit and mask method did. This will enable an improved analysis to the differences in the radiative field regarding both the internal and external cloud heterogeneity. The radiative transfer calculations can also be expanded to include an ICA calculation to study the impact of horizontal photon flow for both the mask and the fit method. In order to compensate for the degree of bias in the satellite data, the radiative transfer simulations will be conducted over a large range of differing cloud heterogeneities, solar zenith angles, and sensor zenith angles as suggested in Di Girolamo et al. (2010).

Potential work can also include the incorporation of microwave satellites such as AMSR-E or SMM/I to provide datasets to compare and validate the MODIS estimates.

References

Ackerman, Steven A., et al. "Discriminating clear sky from clouds with MODIS." Journal of Geophysical Research: Atmospheres (1984–2012) 103.D24 (1998): 32141-32157.

Ackerman, Steve, et al. "Discriminating clear-sky from cloud with MODIS algorithm theoretical basis document (MOD35." *MODIS Cloud Mask Team, Cooperative Institute for Meteorological Satellite Studies, University of Wisconsin* (2010).

Barker, Howard W., and John A. Davies. "Solar radiative fluxes for stochastic, scale-invariant broken cloud fields." Journal of the Atmospheric Sciences 49.13 (1992): 1115-1126.

Barker, Howard W., Bruce A. Wiellicki, and Lindsay Parker. "A parameterization for computing grid-averaged solar fluxes for inhomogeneous marine boundary layer clouds. Part II: Validation using satellite data." Journal of the atmospheric sciences 53.16 (1996): 2304-2316.

Barker, Howard W., Graeme L. Stephens, and Qiang Fu. "The sensitivity of domain‐averaged solar fluxes to assumptions about cloud geometry." Quarterly Journal of the Royal Meteorological Society 125.558 (1999): 2127-2152.

Barker, H. W., and P. Räisänen. "Radiative sensitivities for cloud structural properties that are unresolved by conventional GCMs." Quarterly Journal of the Royal Meteorological Society 131.612 (2005): 3103-3122.

Barker, H. W., et al. "Assessing 1D atmospheric solar radiative transfer models: Interpretation and handling of unresolved clouds." Journal of Climate 16.16 (2003): 2676-2699.

Bennartz, Ralf. "Global assessment of marine boundary layer cloud droplet number concentration from satellite." Journal of Geophysical Research: Atmospheres (1984–2012) 112.D2 (2007).

Cahalan, Robert F., et al. "Independent pixel and Monte Carlo estimates of stratocumulus albedo." Journal of the Atmospheric Sciences 51.24 (1994): 3776-3790.

Cahalan, R. F., W. Ridgeway, W. J. Wiscombe, S. Gollmer, and Harshvardhan, 1994b: Independent Pixel and Monte Carlo Estimates of Stratocumulus Albedo. *Journal of Atmospheric Sciences*, **51**, 3776–3790.

Considine, Geoffrey, Judith A. Curry, and Bruce Wielicki. "Modeling cloud fraction and horizontal variability in marine boundary layer clouds." Journal of Geophysical Research: Atmospheres (1984–2012) 102.D12 (1997): 13517-13525.

Foster, Michael J., Ralf Bennartz, and Andrew Heidinger. "Estimation of liquid cloud properties that conserve total-scene reflectance using satellite measurements." Journal of Applied Meteorology and Climatology 50.1 (2011): 96-109.

Fu, Qiang, B. Carlin, and G. Mace. "Cirrus horizontal inhomogeneity and OLR bias." Geophysical research letters 27.20 (2000): 3341-3344.

Genkova, Iliana, and Roger Davies. "Spatial heterogeneity of reflected radiance from globally distributed clouds." Geophysical research letters 30.21 (2003).

Di Girolamo, Larry, Lusheng Liang, and Steven Platnick. "A global view of one‐dimensional solar radiative transfer through oceanic water clouds." Geophysical Research Letters 37.18 (2010).

Di Giuseppe, F., and A. M. Tompkins. "Effect of spatial organization on solar radiative transfer in three-dimensional idealized stratocumulus cloud fields." Journal of the atmospheric sciences 60.15 (2003): 1774-1794..

Di Giuseppe, F., and A. M. Tompkins. "Impact of cloud cover on solar radiative biases in deep convective regimes." Journal of the atmospheric sciences 62.6 (2005): 1989-2000.

Grosvenor, D. P., and R. Wood, 2014: The effect of solar zenith angle on MODIS cloud optical and microphysical retrievals within marine liquid water clouds. *Atmospheric Chemistry and Physics*, **14**, 7291–7321, doi:10.5194/acp-14-7291-2014. http://www.atmos-chem-phys.net/14/7291/2014/.

Ham, Seung‐Hee, et al. "Effects of 3‐D clouds on atmospheric transmission of solar radiation: Cloud type dependencies inferred from A‐train satellite data." Journal of Geophysical Research: Atmospheres 119.2 (2014): 943-963.

Heidinger, Andrew K., et al. "The pathfinder atmospheres-extended avhrr climate dataset." Bulletin of the American Meteorological Society 95.6 (2014): 909-922..

Horváth, Akos, and Roger Davies. "Anisotropy of water cloud reflectance: A comparison of measurements and 1D theory." Geophysical Research Letters 31.1 (2004).

Horváth, Ákos, Chellappan Seethala, and Hartwig Deneke. "View angle dependence of MODIS liquid water path retrievals in warm oceanic clouds." Journal of Geophysical Research: Atmospheres 119.13 (2014): 8304-8328.

Kato, Seiji, and Alexander Marshak. "Solar zenith and viewing geometry‐dependent errors in satellite retrieved cloud optical thickness: Marine stratocumulus case." Journal of Geophysical Research: Atmospheres (1984–2012) 114.D1 (2009).

Kato, Seiji, Laura M. Hinkelman, and Anning Cheng. "Estimate of satellite‐derived cloud optical thickness and effective radius errors and their effect on computed domain‐averaged irradiances." Journal of Geophysical Research: Atmospheres (1984–2012) 111.D17 (2006).

King, Michael D., et al. "Cloud Retrieval Algorithms for MODIS: Optical Thickness." Effective Particle Radius, and Thermodynamic Phase, Products 6 (1998): L2.

King, Michael D., et al. "Collection 005 change summary for the MODIS cloud optical property (06_OD) algorithm." MODIS Atmosphere (2006): 8.

King, Michael D., et al. "Spatial and temporal distribution of clouds observed by MODIS onboard the Terra and Aqua satellites." Geoscience and Remote Sensing, IEEE Transactions on 51.7 (2013): 3826-3852.

Kobayashi, Takashisa. "Radiative properties of finite cloud fields over a reflecting surface." Journal of the Atmospheric Sciences 46.14 (1989): 2208-2214..

Kobayashi, Takahisa. "Effects due to cloud geometry on biases in the albedo derived from radiance measurements." Journal of climate 6.1 (1993): 120-128..

Koren, I., L. Oreopoulos, G. Feingold, L. A. Remer, and O. Altaratz, 2008: How small is a small cloud? *Atmospheric Chemistry and Physics*, **8**, 3855–3864.

Larson, V. E., R. Wood, P. R. Field, J.-C. Golaz, T. H. Vonder Haar, and W. R. Cotton, 2001: Systematic Biases in the Microphysics and Thermodynamics of Numerical Models That Ignore Subgrid-Scale Variability. *Journal of Atmospheric Sciences*, **58**, 1117–1128.

Liang, Lusheng, Larry Di Girolamo, and Steven Platnick. "View‐angle consistency in reflectance, optical thickness and spherical albedo of marine water‐clouds over the northeastern Pacific through MISR‐MODIS fusion." Geophysical Research Letters 36.9 (2009).

Loeb, Norman G., and Roger Davies. "Observational evidence of plane parallel model biases: Apparent dependence of cloud optical depth on solar zenith angle." Journal of Geophysical Research: Atmospheres (1984–2012) 101.D1 (1996): 1621-1634..

Loeb, Norman G., and J. A. Coakley Jr. "Inference of marine stratus cloud optical depths from satellite measurements: Does 1D theory apply?." Journal of climate 11.2 (1998): 215-233..

Mace, G. G., Q. Zhang, M. Vaughan, R. Marchand, G. Stephens, C. Trepte, and D. Winker, 2009: A description of hydrometeor layer occurrence statistics derived from the first

year of merged Cloudsat and CALIPSO data. *Journal of Geophysical Research*, **114**, 1–17, doi:10.1029/2007JD009755. http://doi.wiley.com/10.1029/2007JD009755.

Maddux, B. C., S. A. Ackerman, and S. Platnick. "Viewing geometry dependencies in MODIS cloud products." Journal of Atmospheric and Oceanic Technology 27.9 (2010): 1519-1528..

Marshak, Alexander, et al. "Biases in shortwave column absorption in the presence of fractal clouds." Journal of climate 11.3 (1998): 431-446.

Morrison, H., and A. Gettelman, 2008: A New Two-Moment Bulk Stratiform Cloud Microphysics Scheme in the Community Atmosphere Model, Version 3 (CAM3). Part I: Description and Numerical Tests. *Journal of Climate*, **21**, 3642–3659, doi:10.1175/2008JCLI2105.1. http://journals.ametsoc.org/doi/abs/10.1175/2008JCLI2105.1.

Naud, C. M., A. Del Genio, G. G. Mace, S. Benson, E. E. Clothiaux, and P. Kollias, 2008: Impact of Dynamics and Atmospheric State on Cloud Vertical Overlap. *Journal of Climate*, **21**, 1758–1770, doi:10.1175/2007JCLI1828.1. http://journals.ametsoc.org/doi/abs/10.1175/2007JCLI1828.1.

O'Hirok, William, and Catherine Gautier. "The impact of model resolution on differences between independent column approximation and Monte Carlo estimates of shortwave surface irradiance and atmospheric heating rate." Journal of the atmospheric sciences 62.8 (2005): 2939-2951..

Oreopoulos, Lazaros, and Roger Davies. "Plane parallel albedo biases from satellite observations. Part II: Parameterizations for bias removal." Journal of climate 11.5 (1998): 933-944.

Oreopoulos, L., et al. "Performance of Goddard earth observing system GCM column radiation models under heterogeneous cloud conditions." Atmospheric research 72.1 (2004): 365-382.

Oreopoulos, Lazaros, Robert F. Cahalan, and Steven Platnick. "The plane-parallel albedo bias of liquid clouds from MODIS observations." Journal of Climate 20.20 (2007): 5114-5125.

Petty, G. W., 2008: *A First Course in Atmospheric Thermodynamics*. 1st ed. Sundog Publishing, 337 pp.

Pincus, Robert, and Stephen A. Klein. "Unresolved spatial variability and microphysical process rates in large‐scale models." Journal of Geophysical Research: Atmospheres (1984–2012) 105.D22 (2000): 27059-27065.

Pincus, Robert, and K. Franklin Evans. "Computational cost and accuracy in calculating three-dimensional radiative transfer: Results for new implementations of Monte Carlo and SHDOM." Journal of the Atmospheric Sciences 66.10 (2009): 3131-3146.

Pincus, R., S. a. McFarlane, and S. a. Klein, 1999: Albedo bias and the horizontal variability of clouds in subtropical marine boundary layers: Observations from ships and satellites. *Journal of Geophysical Research*, **104**, 6183, doi:10.1029/1998JD200125. http://doi.wiley.com/10.1029/1998JD200125.

Räisänen, P., H. W. Barker, M. F. Khairoutdinov, J. Li, and D. a. Randall, 2004: Stochastic generation of subgrid-scale cloudy columns for large-scale models. *Quarterly Journal of the Royal Meteorological Society*, **130**, 2047–2067, doi:10.1256/qj.03.99. http://doi.wiley.com/10.1256/qj.03.99.

Salzmann, M., Y. Ming, J.-C. Golaz, P. a. Ginoux, H. Morrison, a. Gettelman, M. Krämer, and L. J. Donner, 2010: Two-moment bulk stratiform cloud microphysics in the GFDL AM3 GCM: description, evaluation, and sensitivity tests. *Atmospheric Chemistry and Physics*, **10**, 8037–8064, doi:10.5194/acp-10-8037-2010. http://www.atmos-chem-phys.net/10/8037/2010/.

Siebesma, A. P., and Coauthors, 2003: A Large Eddy Simulation Intercomparison Study of Shallow Cumulus Convection. *Journal of Atmospheric Sciences*, **60**, 1201–1219.

Stevens, B., and Coauthors, 2005: Evaluation of Large-Eddy Simulations via Observations of Nocturnal Marine Stratocumulus. *Monthly Weather Review*, **133**, 1443–1462.

Várnai, Tamás, and Alexander Marshak. "View angle dependence of cloud optical thicknesses retrieved by Moderate Resolution Imaging Spectroradiometer (MODIS)." Journal of Geophysical Research: Atmospheres (1984–2012) 112.D6 (2007).

Webb, M. J., F. H. Lambert, and J. M. Gregory, 2013: Origins of differences in climate sensitivity, forcing and feedback in climate models. *Climate Dynamics*, **40**, 677–707, doi:10.1007/s00382-012-1336-x. http://link.springer.com/10.1007/s00382-012-1336-x.

Wood, Robert, and Dennis L. Hartmann. "Spatial variability of liquid water path in marine low cloud: The importance of mesoscale cellular convection." Journal of climate 19.9 (2006): 1748-1764..

Zuev, Vladimir E., and Georgii A. Titov. "Radiative transfer in cloud fields with random geometry." Journal of the atmospheric sciences 52.2 (1995): 176-190.